NOAA ATLAS No. 6

Atlas of Outgoing Longwave Radiation Derived from NOAA Satellite Data

Silver Spring, Md.
January 1985

U.S. DEPARTMENT OF COMMERCE
National Oceanic and Atmospheric Administration
National Weather Service
National Environmental Satellite Data and Information Service

NOAA ATLAS No. 6

Atlas of Outgoing Longwave Radiation Derived from NOAA Satellite Data

John E. Janowiak, A.F. Krueger, and P.A. Arkin
Climate Analysis Center
National Meteorological Center
National Weather Service
and
Arnold Gruber
Atmospheric Sciences Branch
Climate and Earth Sciences Laboratory
National Environmental Satellite Data and Information Service

Silver Spring, Md.
January 1985

U.S. DEPARTMENT OF COMMERCE
Malcolm Baldrige, Secretary

National Oceanic and Atmospheric Administration
Anthony J. Calio, Acting Administrator

National Weather Service
Richard E. Hallgren, Director

National Environmental Satellite Data and Information Service
John H. Mc Elroy, Director

Table of Contents

	Page
Abstract	1
1. Introduction	1
2. Changes in satellites and procedures	1
3. Discussion of seasonal grand means and average standard deviations	3
References	6
Table	7
Figures	8

Atlas of Outgoing Longwave Radiation Derived From NOAA Satellite Data

ABSTRACT

An atlas of monthly and seasonal grand means and average standard deviations of outgoing longwave radiation (OLR) is presented. These statistics were computed using data derived from the NOAA polar orbiting satellites during the period June, 1974 through November, 1983. Corrections for differing sensor characteristics were applied, and the twice daily observations were averaged to minimize diurnal differences, in order to ensure the homogeneity of the data. Although these data are available globally with 2.5° latitude-longitude resolution, we focus our discussion on the tropical and sub-tropical regions where the OLR is highly correlated with cloudiness and precipitation.

1. INTRODUCTION

This atlas contains monthly and seasonal averages and the corresponding standard deviations for the outgoing longwave radiation (OLR) estimated at the top of the atmosphere. It represents an update of the description of this component of the radiation balance that was presented by Winston et al. (1979). That atlas consisted of nearly four years of satellite radiation measurements. The averages presented in this atlas include outgoing longwave radiation data from the original record, and, in addition, measurements from TIROS N, NOAA 6, and NOAA 7. The period making up this new base period extends from June 1974 through November 1983. However, there is a ten-month gap in this record extending from March to December 1978, during which no satellite observations were available due to the failure of NOAA 5. Figure 1 and Table 1 indicate the length of this data set as well as the amount of data contributed by each of the satellites. Note that TIROS N, with 13 months, is the shortest subset of our record. Except for the spring months and the month of December, this record consists of nine years of data.

This atlas presents only the OLR observations. Absorbed solar radiation and albedo, which were contained in the earlier atlas (Winston et al., 1979), require further analysis prior to publication.

2. CHANGES IN SATELLITES AND PROCEDURES

More than four years of satellite derived OLR data have been added to the data set since the first atlas was published. Unfortunately, the new observations are not strictly comparable with the earlier scanning radiometer measurements as presented by Winston et al. (1979). This is due to two types of changes that have taken place on the recent polar-orbiting satellites.

First, the time of day that each satellite crossed the equator differed with each spacecraft . Originally, these times were at 9:00 AM and PM, local time, but with TIROS N they were changed to 3:30 AM and PM. When NOAA 6 was launched, they became 7:30 AM and PM, and finally were changed to 2:30 AM and PM on NOAA 7. Table 1 shows the number of measurements that make up each of the subsets of this record.

Second, the water vapor window channel, from which these measurements have been obtained, has not remained the same on all the satellites that make up this data set. Originally, the scanning radiometer series (June 1974-Feb. 1978) had a broad window extending from 10.5 - 12.5 μm. On TIROS N and NOAA 6 it was decreased to 10.5 - 11.5 μm, while on NOAA 7 it was shifted upward to 11.5 - 12.5 μm. The spectral responses of these filters are shown in Fig. 2.

These data have been maintained as a component of the earth-atmosphere radiation balance since June 1974. An algorithm was developed to convert these window channel measurements to the total OLR. Originally this was done with an algorithm developed by Wark et al. (1962), but the process has been revised several times since then (Abel and Gruber 1979, Ellingson and Ferraro 1983). Recently Ohring et al. (1984) reviewed the entire procedure and concluded that this outgoing longwave radiation record had a positive bias of about 13 W m^{-2}. This conclusion was based on an analysis of simultaneous measurements from NIMBUS 7 of both the total longwave radiation flux (ERB) and the radiance in the 10-12 μm infrared window (THIR). An improved algorithm for converting the window radiance to the total outgoing flux was then derived and was introduced operationally on March 1, 1983. This algorithm is

$$T_F = (a + b\, T_{THIR})\, T_{THIR} \qquad (1)$$

where T_F is the flux temperature, T_{THIR} is the window temperature, a = 1.2149 and b = 1.055×10^{-3}. This in turn is converted to the outgoing longwave flux with the Stephan-Boltzmann Law

$$F = \sigma T_F^4 \qquad (2)$$

The relations among window temperature T_{THIR}, flux temperature T_F, and the outgoing longwave flux F are shown in Fig. 3.

It was also decided to correct the entire record back to June 1974. To do this, however, it was necessary to relate the THIR window radiance to the window radiances of each satellite, e.g. NOAA-SR series, TIROS N, NOAA 6 and NOAA 7. Gruber and Krueger (1984) derived the appropriate equations which were then applied to the entire record.

The equations relating the adjusted flux to the original flux values are

$$F_N = 0.7970\, F_o + 6.357 \times 10^{-4}\, F_o^2 \qquad \text{SR} \qquad (3)$$

$$F_N = 0.8115\, F_o + 5.542 \times 10^{-4}\, F_o^2 \qquad \text{TIROS N/NOAA 6} \qquad (4)$$

$$F_N = 0.8532\, F_o + 3.887 \times 10^{-4}\, F_o^2 \qquad \text{NOAA-7} \qquad (5)$$

where F_N represents the adjusted flux and F_o the original flux values in W m^{-2}. This process has resulted in a more internally consistent record.

The inhomogenity introduced into the record due to changes in equator crossings cannot be easily remedied. Evidence indicates that the OLR undergoes a diurnal cycle that is a function of geography and circulation regime (Gruber and Krueger, 1984; Saunders and Hunt, 1980; Saunders, et al., 1983). Since not enough is presently known about the diurnal cycle to apply a proper correction to each of the data subsets that make up this record, we have attempted to minimize this effect by averaging the day and night observations.

We believe that the main features of the OLR and their variation in space and time are well represented by this data set. Consequently, we anticipate that it will continue to be of considerable use in the diagnosis of the general circulation and the earth-atmosphere longwave radiation.

3. DISCUSSION OF SEASONAL GRAND MEANS AND AVERAGE STANDARD DEVIATIONS

The OLR is largely modulated by temperature and cloudiness. Consequently, its magnitude decreases poleward from about 30° latitude, along with temperature, in both hemispheres. Since the spatial variation of temperature is small over the tropics, however, the OLR there is largely a function of cloudiness so the two tend to vary inversely. Accordingly, the OLR is lowest over the major convective areas of the tropics where middle and high cloudiness prevail. Conversely, it is relatively high over the tradewind regions of the oceans where the clouds are typically stratocumulus or tradewind cumulus that only extend 1 or 2 kilometers above the surface. The maximum values occur over the deserts where the skies are clear and the surface temperatures are highest. Figs. 4 and 5 show the annual mean and standard deviation of the 12 grand monthly means. Plots of the seasonal and monthly means appear in Figs. 6-21. The large spatial variation, especially with longitude, is impressive over the tropics and occurs in response to the large scale tropical circulation. Some highly persistent features of this circulation are depicted by:

(1) Major convective areas over the tropical continents of South America and Africa as well as over the Indo-Pacific area, where the longwave cooling is as low as 200 W m^{-2}.

(2) Major subsiding areas associated with the oceanic tradewind systems, where the longwave cooling is greater than 260 W m^{-2}. One of the most striking examples is the equatorial Pacific dry zone that extends along the equator from the dateline eastward to South America. This area is particularly significant since its western extremity fluctuates with the southeast trades and the Southern Oscillation. At times it is replaced by extreme cloudiness and rain, and during the 1982-83 El Nino event this dry zone was virtually eliminated.

This atlas also contains the standard deviations of the daily OLR about the seasonal and monthly means (Figs. 22 - 37). These patterns are similar to their respective means with the greatest variability generally associated with the lowest OLR and the smallest variability associated with the largest OLR values. The seasonal variation in this statistic is interesting and will now be described in some detail.

During northern winter (Fig. 9) the Southern Indo-Pacific Convergence Zone (SPCZ) exhibits the greatest variability. The lowest OLR in this region is located over Indonesia-New Guinea while the maximum variability is located to the east. Note the large area of 35 W m^{-2} extending from the Solomon Islands southeastward toward French Polynesia. In South America, the greatest variability occurs over eastern Brazil, while the lowest infrared radiation occurs east of the Andes over the upper Amazon Valley. The extension of relatively high variability across the equator towards Africa is associated with frequent altostratus-cirrostratus plumes that reach as far as the subtropical jetstream over North Africa and the middle east. Similarily, the roots of the North American subtropical jetstream are found in a region of high variability near 10°N over the eastern Pacific. Note the axis extending northeastward across Mexico, southeastern United States and then out over the Atlantic. South of this jetstream the infrared radiation is high and its variability very low over Central America and the Caribbean, indicating an area of very persistent subsidence. The subtropical jetstream over the North Pacific is indicated by a region of large variability extending along the axis of this current with larger values occurring at the exit region, suggesting a tendency for enhanced transient eddy activity there. Over the western Pacific and south of this jetstream an area of low variability (σ = 15 W m^{-2}) is indicated and is associated with the northeast trades. This area expands and contracts longitudinally with fluctuations in the North Pacific subtropical jetstream. The equatorial Pacific dry zone is depicted by an area of high OLR (260 W m^{-2}) and low variability (σ = 15 W m^{-2}) extending from near the dateline eastward to South America. This region corresponds to the location of the Pacific southeast trade winds. The increased variability at the western edge of this region is a manifestation of interludes when the SPCZ shifts northeastward in association with a weakening of the southeast trades.

During northern spring (Fig. 6) the maximum variability is still located east of New Guinea with a southeastward extension into the South Pacific. However, another maximum begins to appear in the Bay of Bengal and is associated with the northward migration of the monsoon into southeast Asia. An interesting feature, found during this season only, is an axis of enhanced variability south of the equator and extending from 180° to 120°W. It extends directly into the western portion of the dry zone. Note that the spring average itself does not show this feature. This is the South Pacific ITCZ which appears as a very transitory feature occurring only during this season in contrast to the ITCZ north of the equator where the variability is 50% greater. It is during this season that the sea surface temperatures in the south equatorial current reach their maximum, possibly contributing to the enhanced convection and hence, variability, that occurs at this time. Two regions of large variability appear over the northern continents this season. One is over the lower Mississippi Valley, the other over Eurasia near the Caspian Sea. Both reflect enhanced spring storminess over these regions. But in addition, they reflect the large upward trend in outgoing longwave radiation that sets in during spring due to the strong surface heating. Near the Caspian Sea, for example, the radiation rises from 220 W m^{-2} during winter to 300 W m^{-2} during summer.

By northern summer (Fig. 7) the major tropical convergence regions have moved into the Northern Hemisphere. Note the large variability associated with the northern ITCZ over the Pacific, the Atlantic and Africa. The maximum variability, however, is associated with the southeast Asian monsoon. Not only is it largest over the

Bay of Bengal and the Philippines, but it is very large over most of the western Pacific. Concurrently, the northern subtropical anticyclones are strong during this season and are associated with large areas of very low variability (σ = 10 W m^{-2}) over the eastern Pacific and Atlantic. It is of interest that, south of the equator, the winter storm tracks are indicated by the large variability between 30-40°S over both the Pacific and Atlantic.

During Autumn there is a diminution in the variability in OLR over the Indian subcontinent as the monsoon begins to withdraw, but it remains large over most of the Northern Hemisphere tropics. Note the large variability, not only in the northern ITCZ, but also over the western Pacific and Bay of Bengal. South of the equator, the variability associated with the SPCZ as well as that associated with the convection over South America and southern Africa begins to increase as the tropical rains set in again over these regions. Yet it is during this season that the equatorial Pacific dry zone is best developed and extends farthest to the west.

The authors wish to express their thanks to Ms. Gail Lucas for typing this manuscript, and to Mr. John Kopman for his assistance in preparing the figures.

REFERENCES

Abel, P. and A. Gruber, 1979: An improved model for the calculation of longwave flux at 11 μm NOAA Tech. Rept. NESS 106, 24 pp.

Ellingson, R.G. and R.R. Ferraro, Jr., 1983: An examination of a technique for estimating longwave radiation budget from satellite radiance observations. J. Clim. & Appl. Met., 22, 1416-1423.

Gruber, A., Irwin Ruff and Charles Earnest, 1983: Determination of the planetary radiation budget from TIROS-N Satellites. NOAA Technical Rpt. NESDIS 3, U.S. Dept. of Commerce, NOAA/NESDIS, Washington, D.C., 12 pp.(NTIS PB84 100916).

Gruber, A. and Krueger A.F. 1984: The status of the NOAA outgoing longwave radiation data set. Bull. Amer. Meteor. Soc., 65, 958-962.

Ohring, G., A. Gruber, R.G. Ellingson, 1984: Satellite determination of the relationship between total longwave radiation flux and infrared window radiance. J. Clim. & Applied Meteor., 23, 416-425.

Saunders, R.W. and G.E. Hunt, 1980: METEOSAT observations of diurnal variation of radiation budget parameters. Nature, 283, 645-647.

_____, L.L. Stowe,G.E. Hunt and C.F. England, 1983: An intercomparison between radiation budget estimates from METEOSAT 1, NIMBUS 7 and TIROS-N satellites. J. Clim and Appl. Met., 22 546-559.

Wark, D.Q., G. Yamomoto, and J. Lienesch, 1962: Infrared flux and surface temperature determination from TIROS radiometer measurements. MSL Rpt. No.10, U.S. Department of Commerce, Weather Bureau.

Winston, J.S., A. Gruber, T. I. Gray, Jr., M.S. Varnadore, D.L. Earnest, and L.P. Mannello, 1979: Earth-atmosphere radiation budget analysis derived from NOAA satellite data, June 1974-February 1978, Vols. 1 and 2, NOAA U.S. Dept. of Commerce, 34 pp.

TABLE I

SATELLITE	EQUATOR CROSSING (LOCAL TIME)	PERIOD OF RECORD	NUMBER OF MONTHS
NOAA SR SERIES (NOAA 2,3,4,5,)	9:00 am, 9:00 pm	6/74 - 2/78	45
TIROS N	3:30 am, 3:30 pm	1/79 - 1/80	13
NOAA - 6	7:30 am, 7:30 pm	2/80 - 8/81	19
NOAA - 7*	2:30 am, 2:30 pm	9/81 - 11/83	27
			104

*Data from this satellite continues to be archived at the time of this publication.

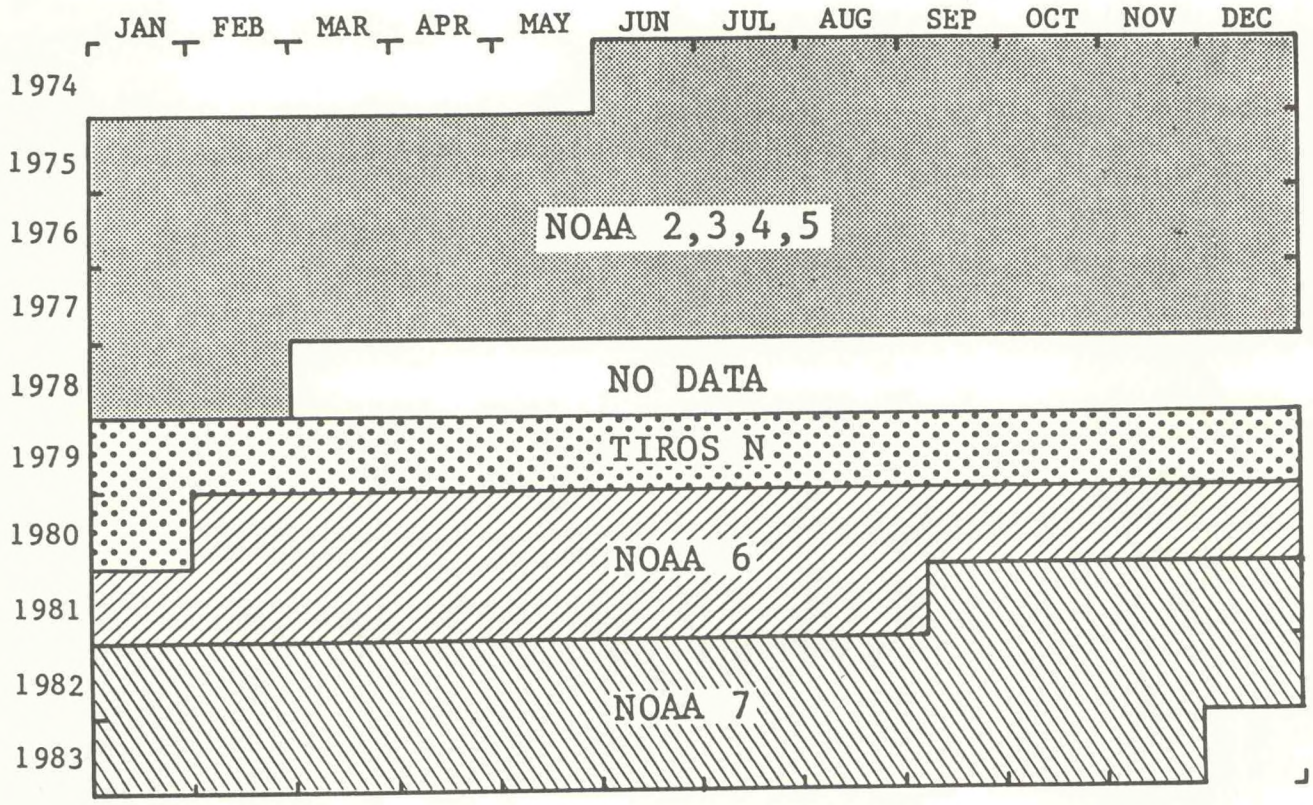

Figure 1. Time history showing the contributions of the 4 NOAA polar orbiting satellites that were used to compute the 9 year base period means.

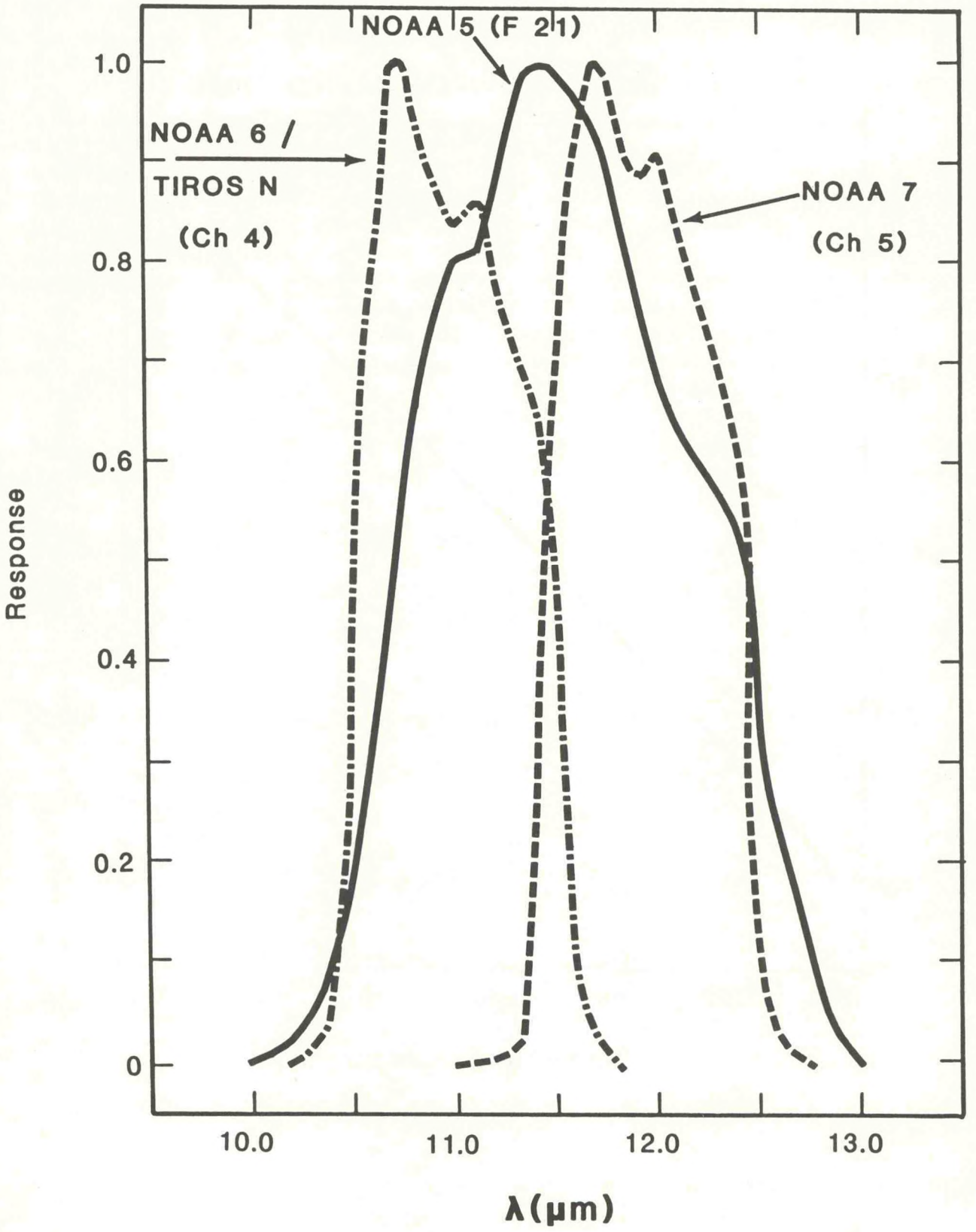

Figure 2. Spectral responses of the water vapor window channel for the 4 satellites used in the 9 year record.

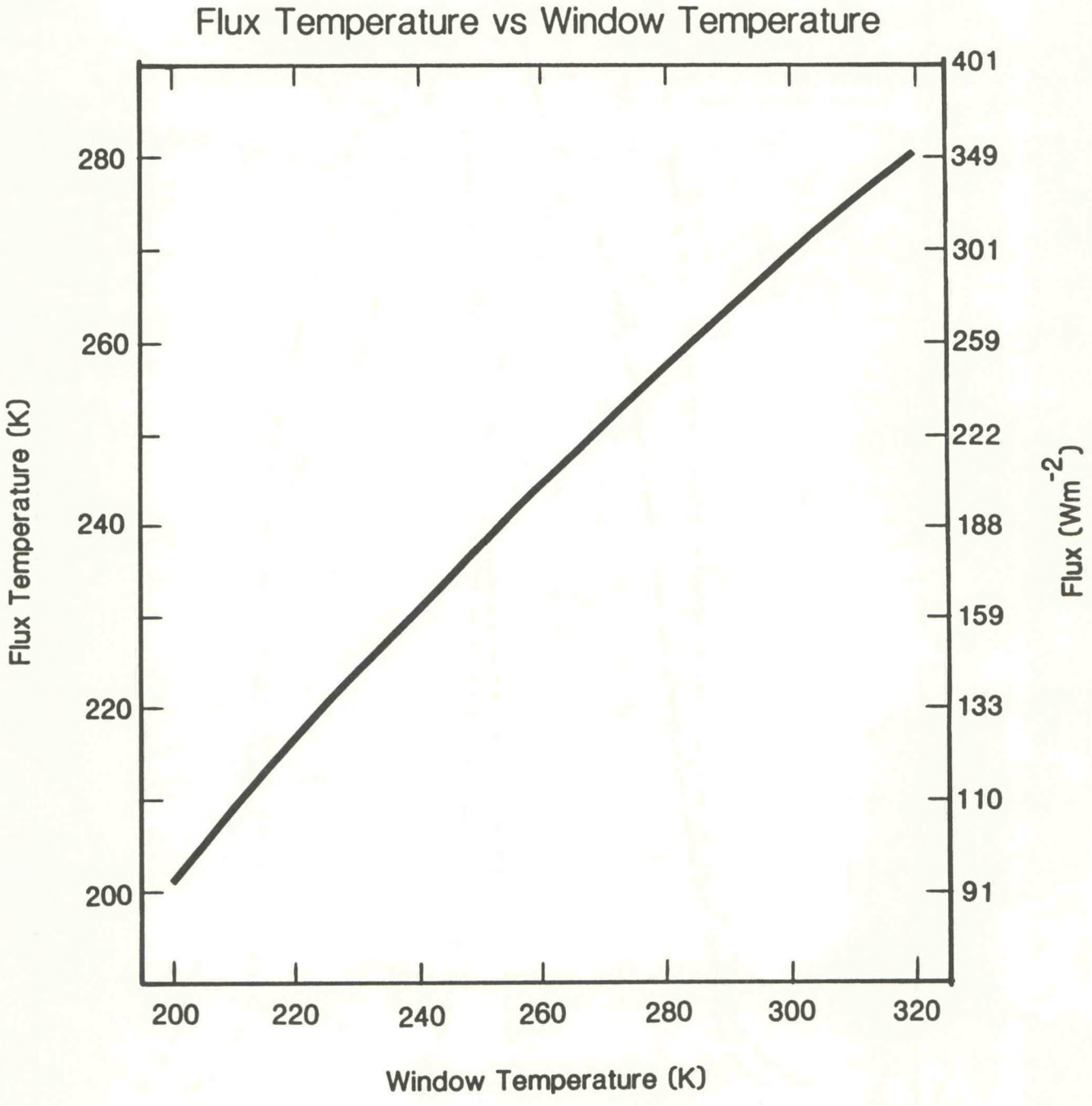

Figure 3. Relationship between window temperature (T_{THIR}) and flux temperature (T_F).

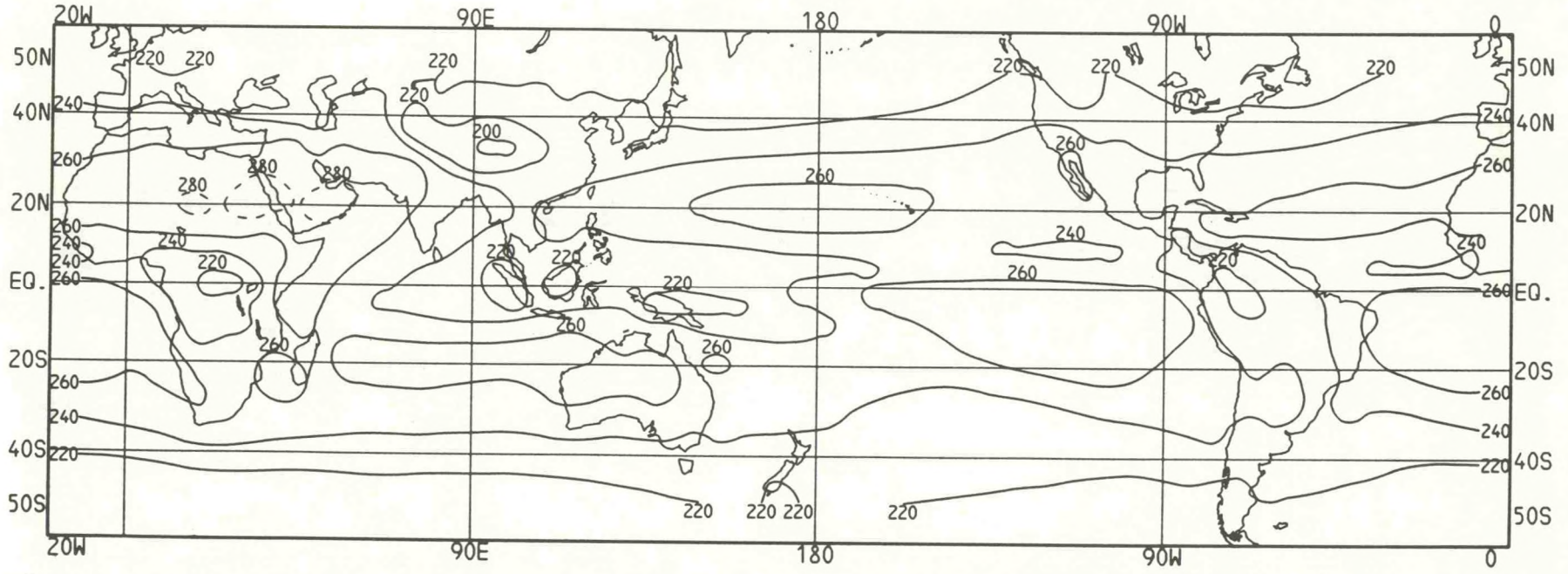

Figure 4. Annual mean of the OLR for the period June, 1974 through November, 1983. The contour interval, is 20 W m^{-2}, with values > 280 W m^{-2} dashed. The day and night observations have been averaged.

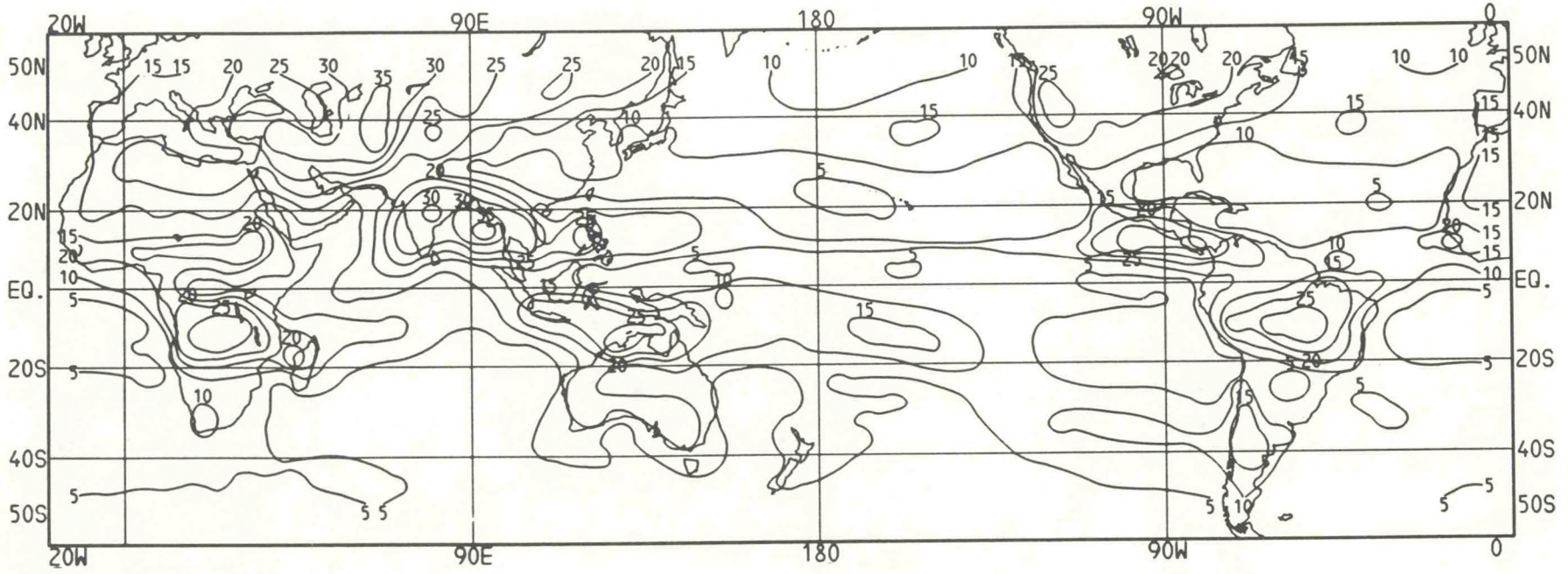

Figure 5. Standard deviation of the 12 grand monthly means of the OLR for the period June, 1974 through November, 1983. The contour interval is 5 W m^{-2}. The day and night observations have been averaged.

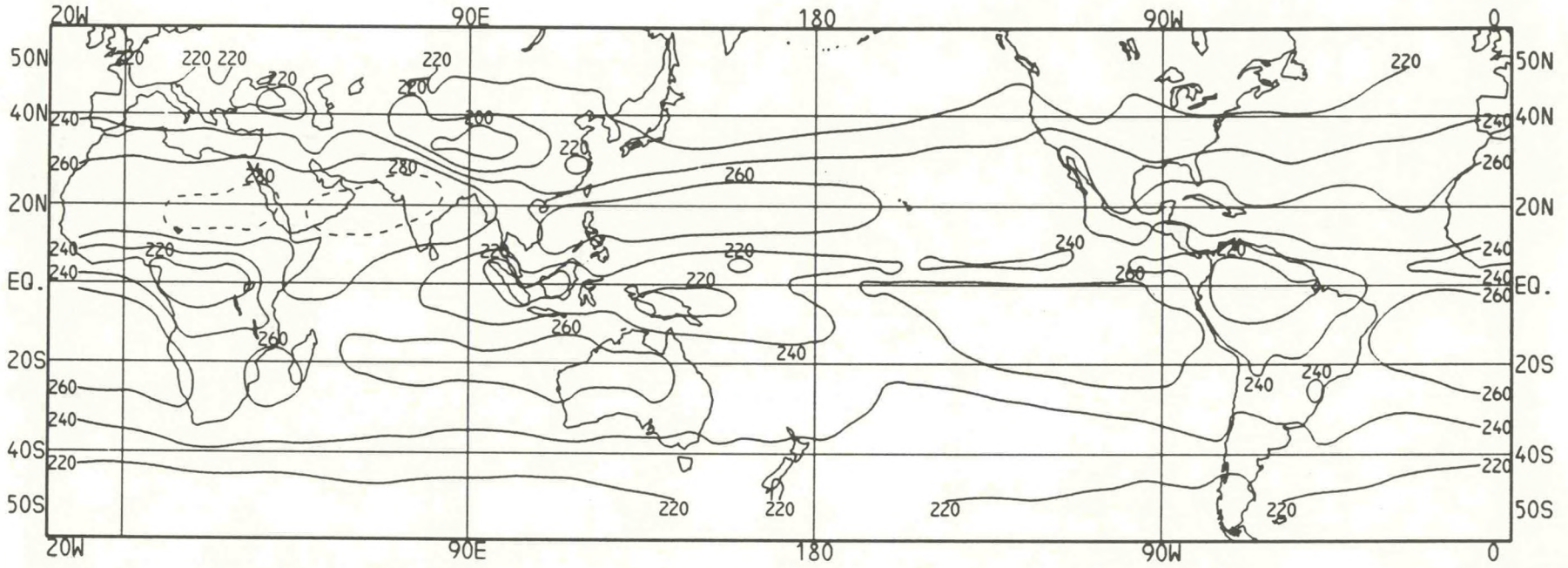

Figure 6. Mean spring season OLR for the period June, 1974 through November, 1983. The contour interval is 20 W m^{-2}, with values > 280 W m^{-2} dashed. The day and night observations have been averaged.

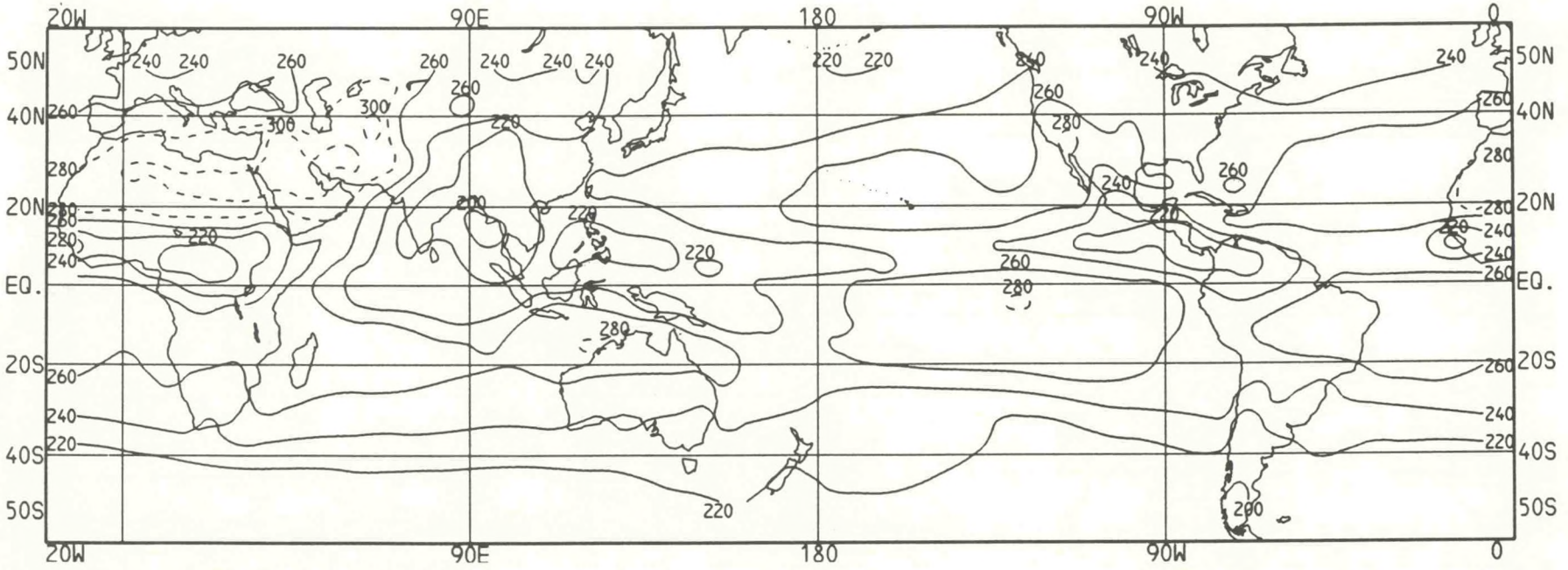

Figure 7. Same as Figure 6, except for summer season.

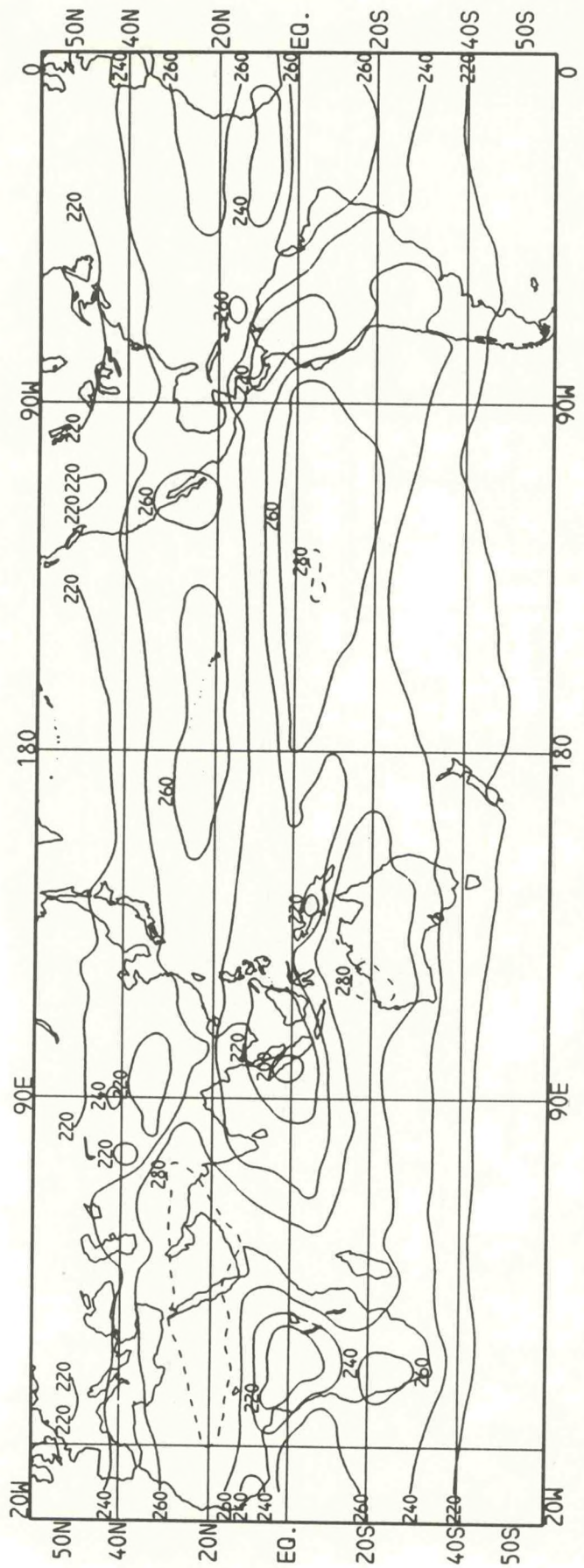

Figure 8. Same as Figure 6, except for autumn season.

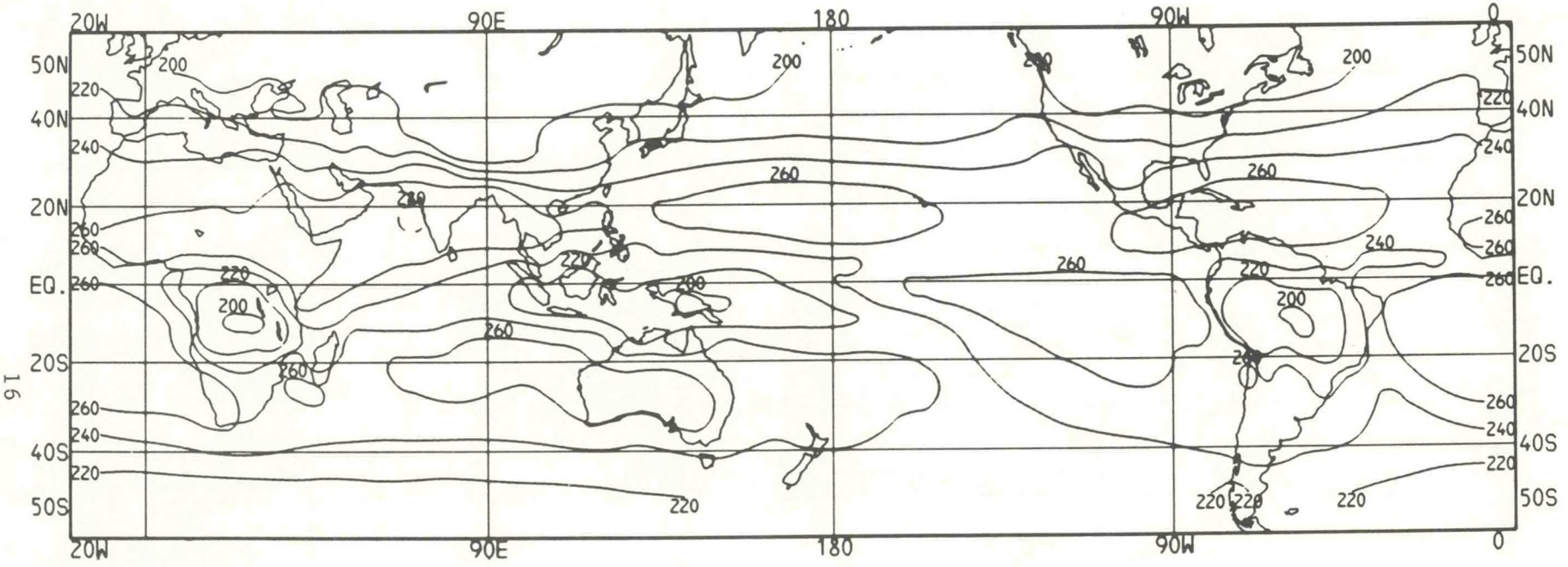

Figure 9. Same as Figure 6, except for winter season

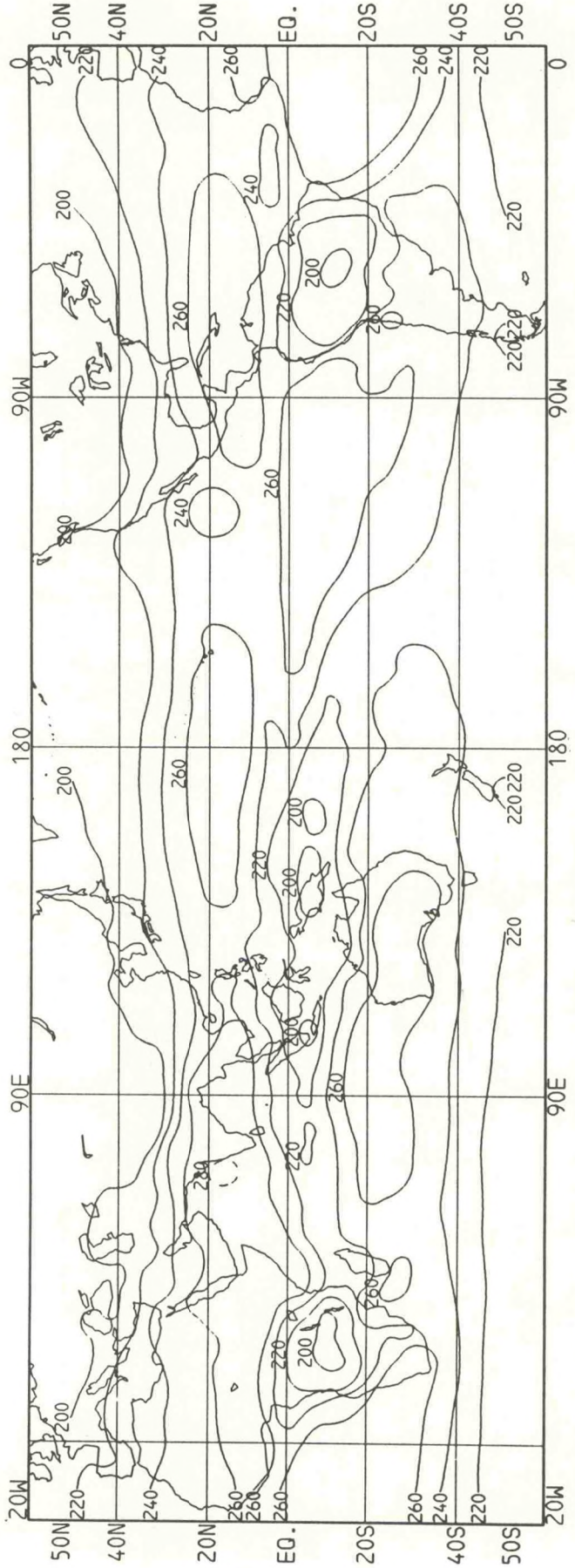

Figure 10. Same as Figure 6, except for January.

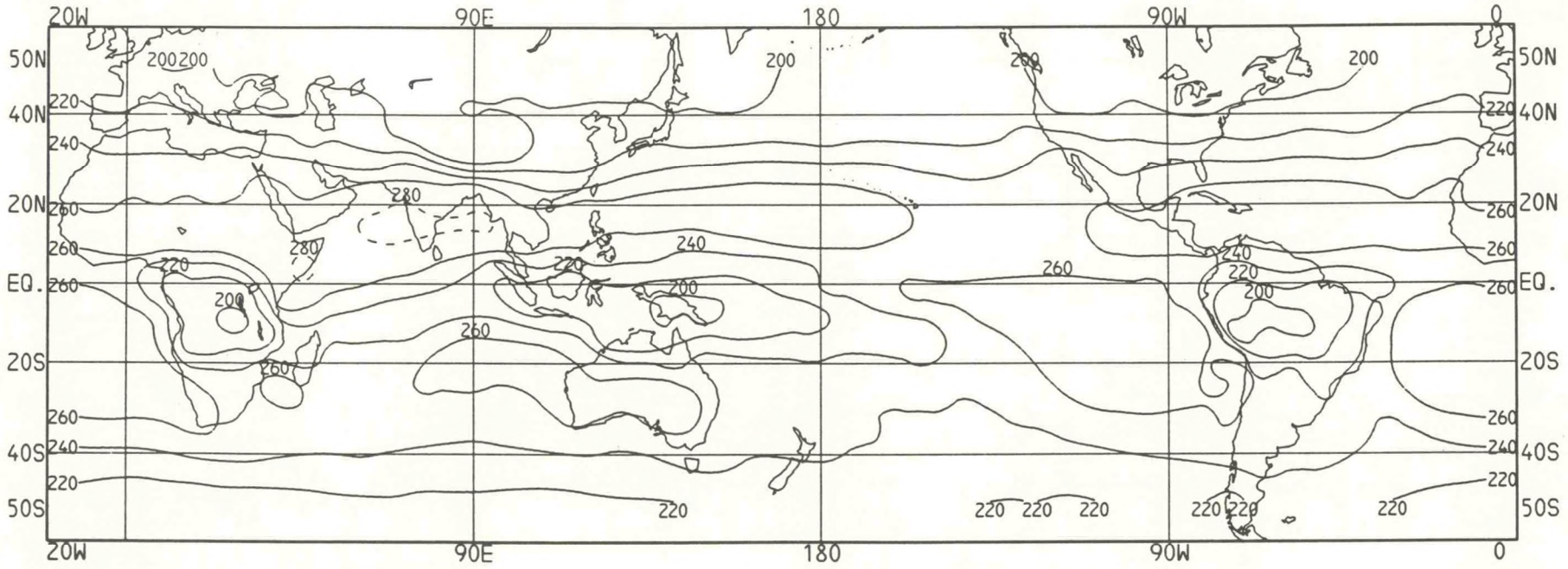

Figure 11. Same as Figure 6, except for Febuary.

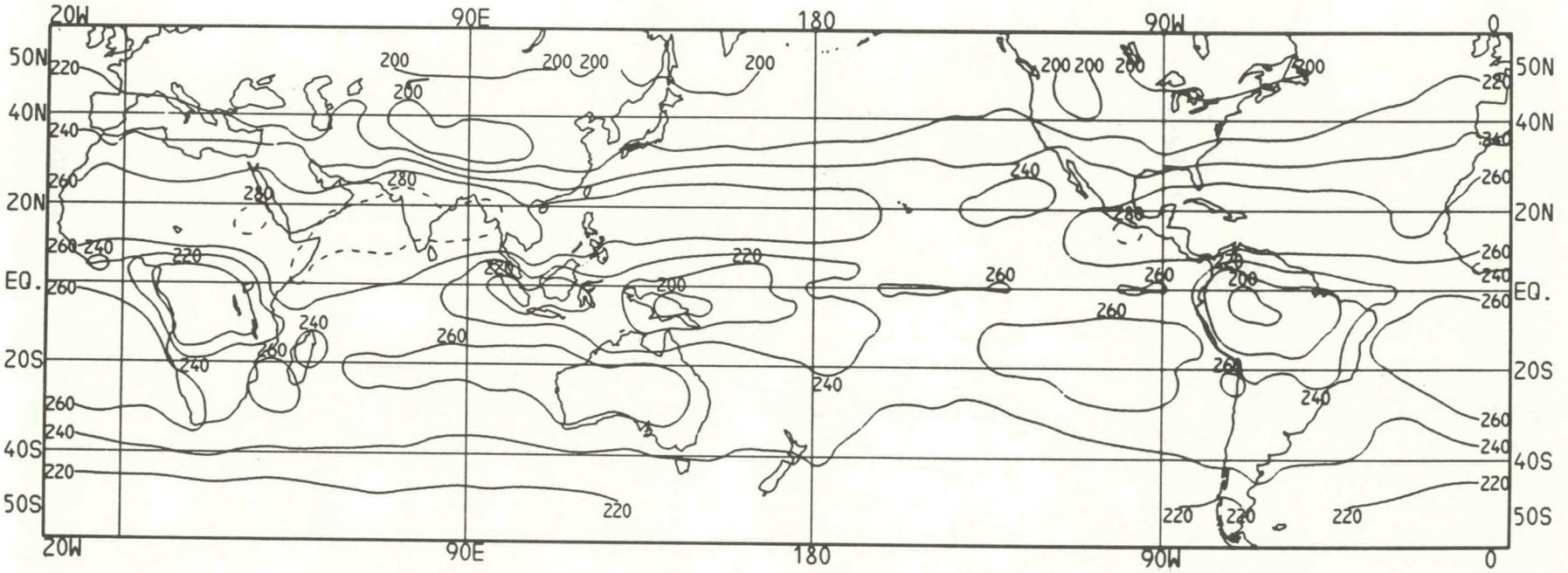

Figure 12. Same as Figure 6, except for March.

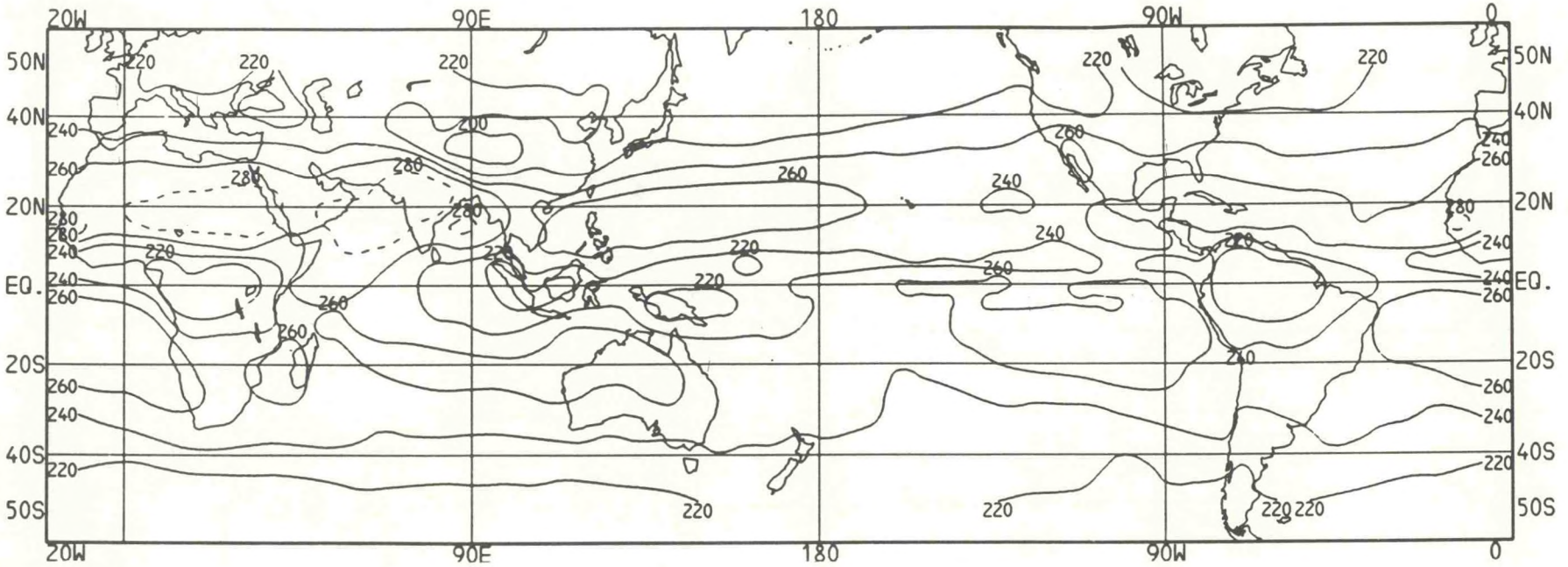

Figure 13. Same as Figure 6, except for April.

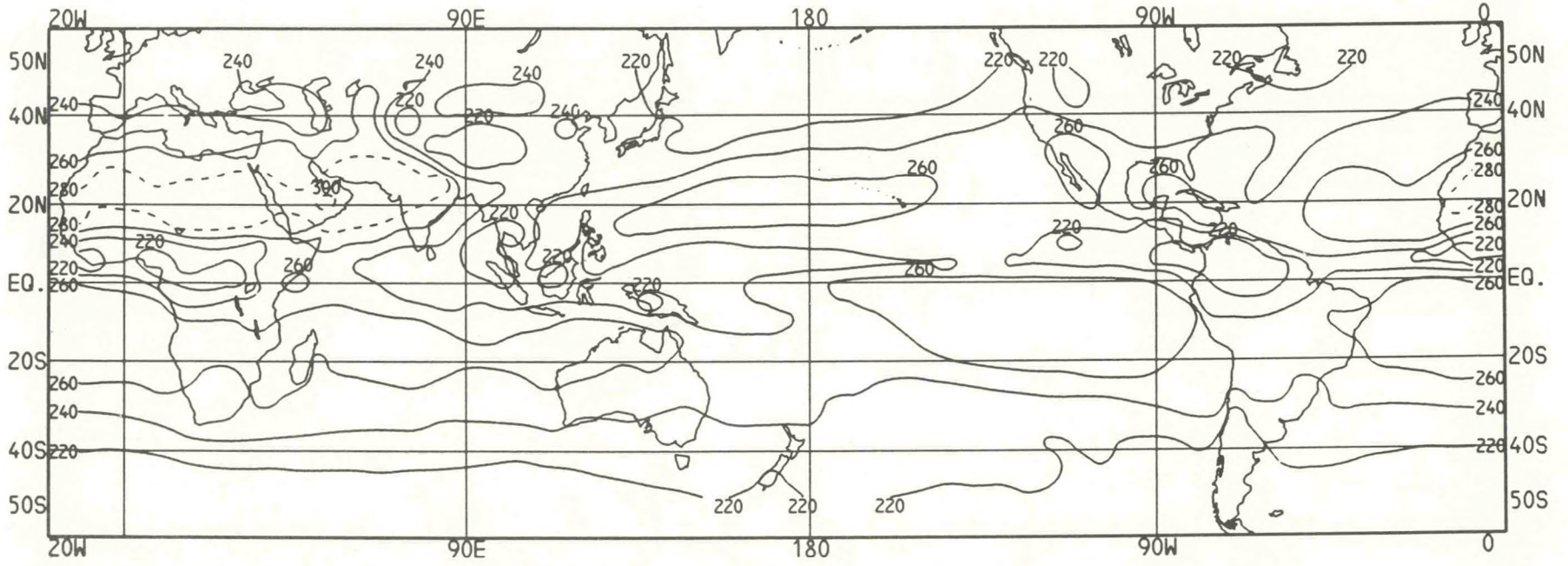

Figure 14. Same as Figure 6, except for May.

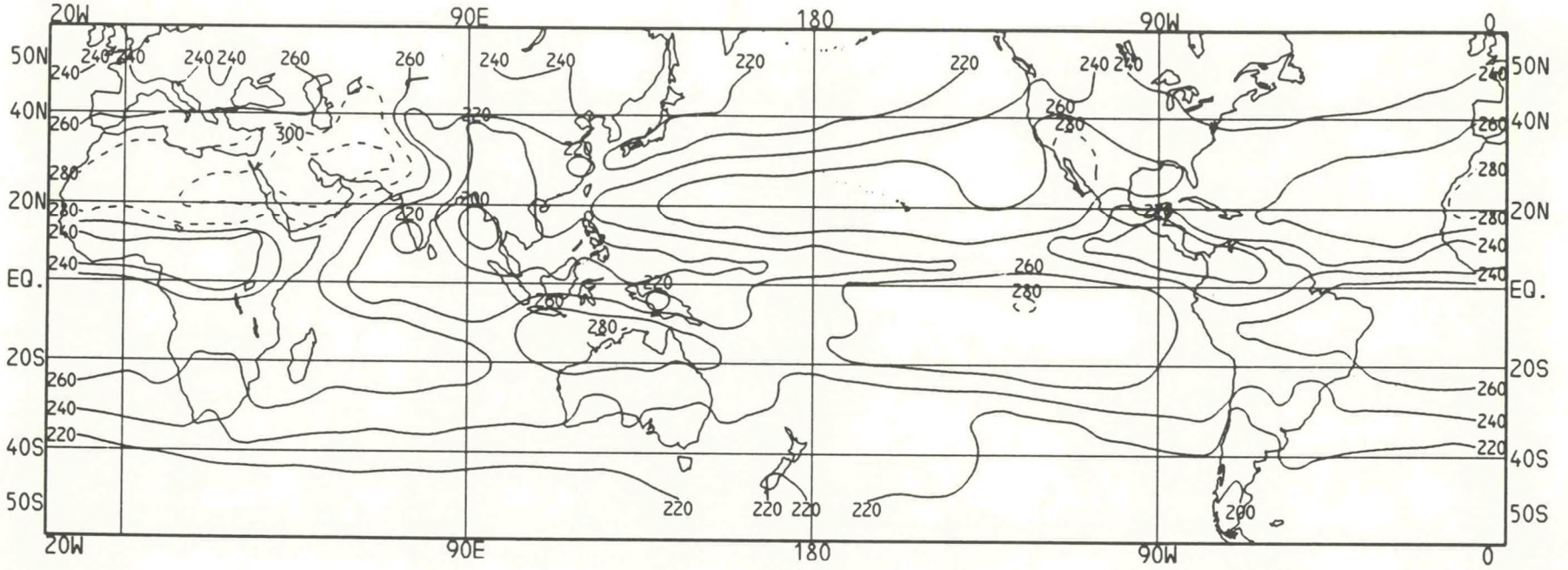

Figure 15. Same as Figure 6, except for June.

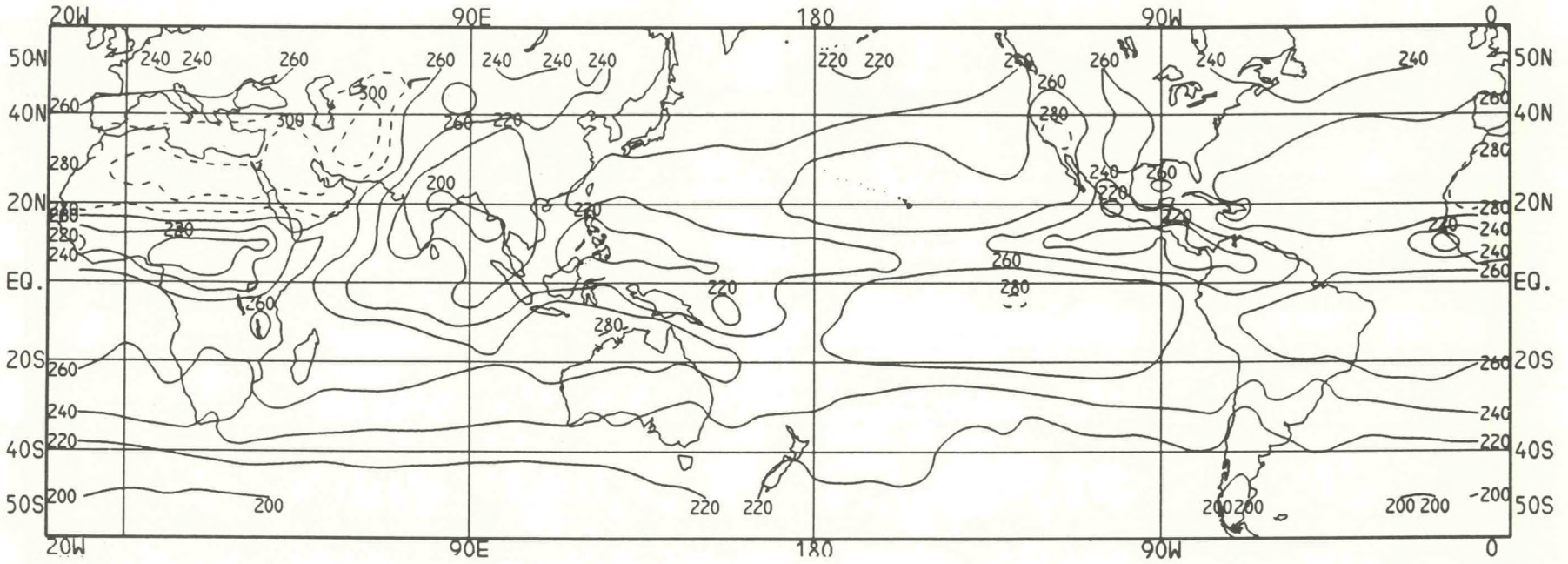

Figure 16. Same as Figure 6, except for July.

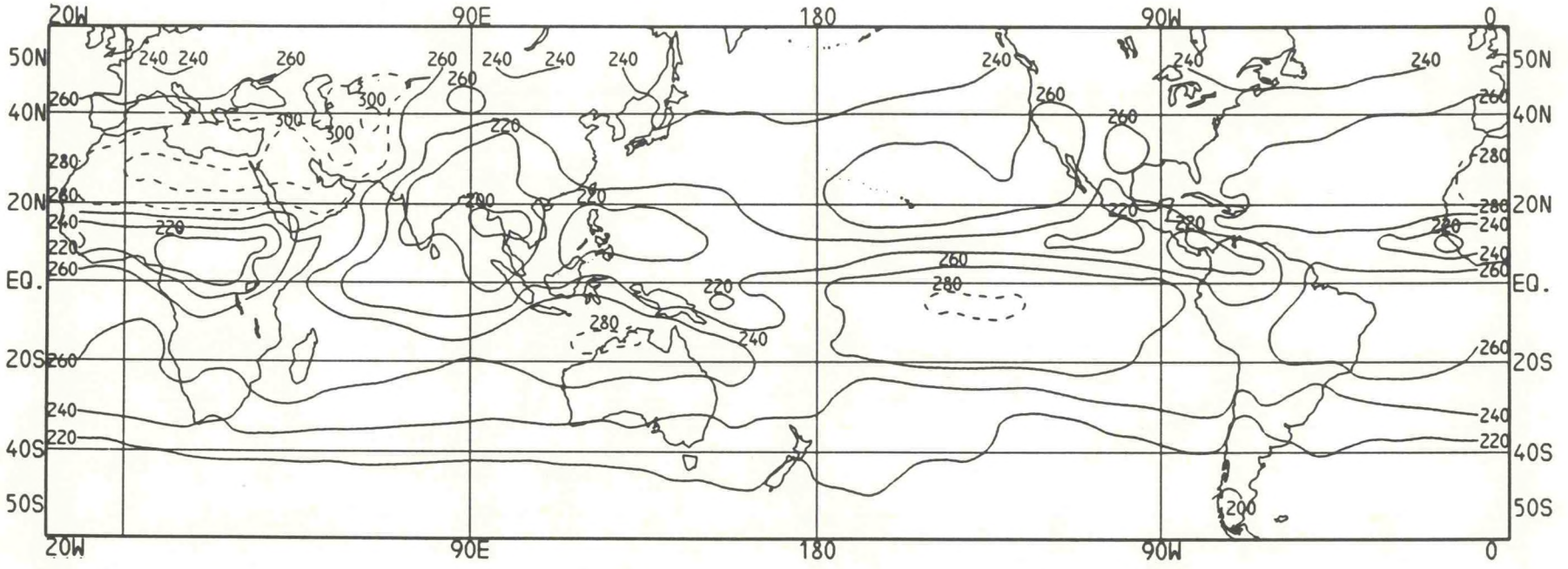

Figure 17. Same an Figure 6, except for August.

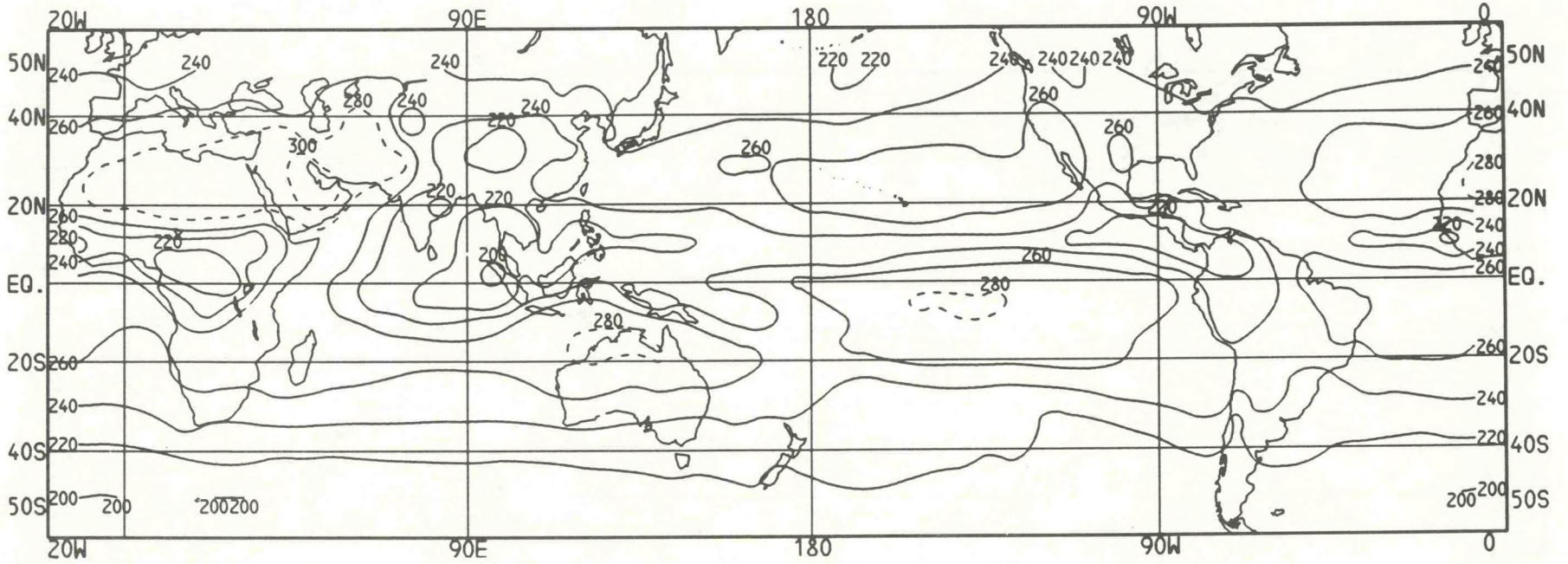

Figure 18. Same as Figure 6, except for September

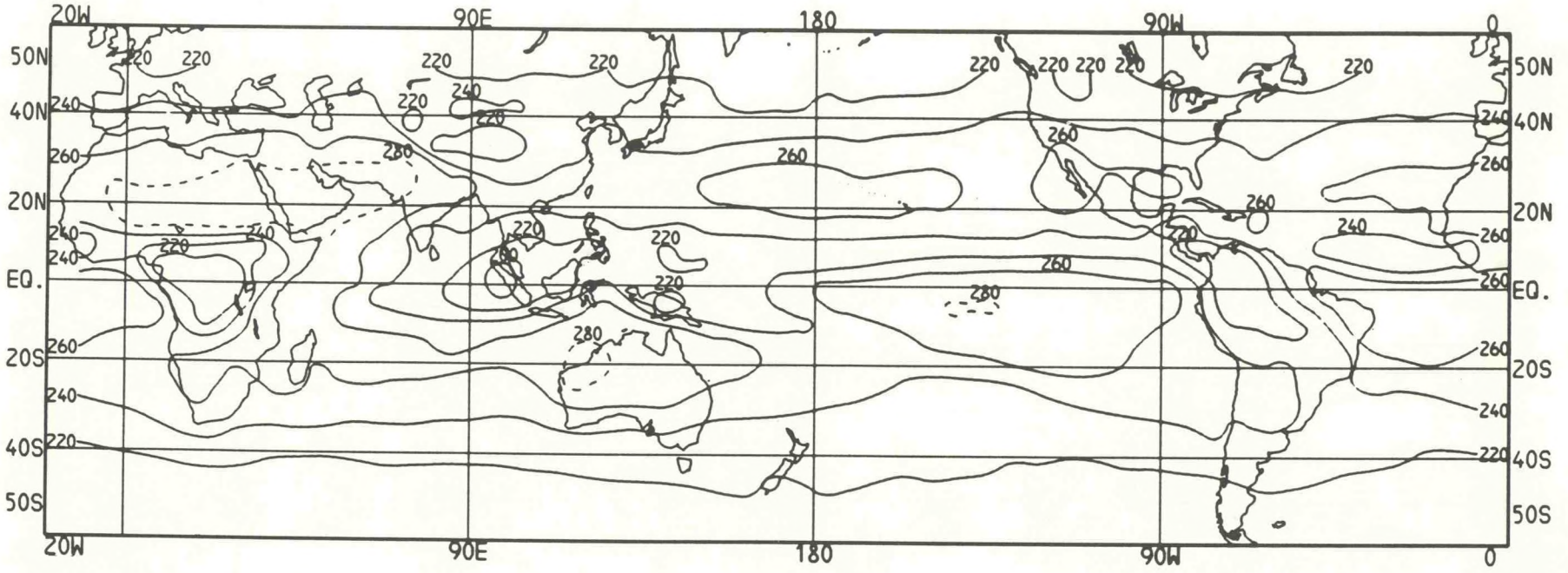

Figure 19. Same as Figure 6, except for October.

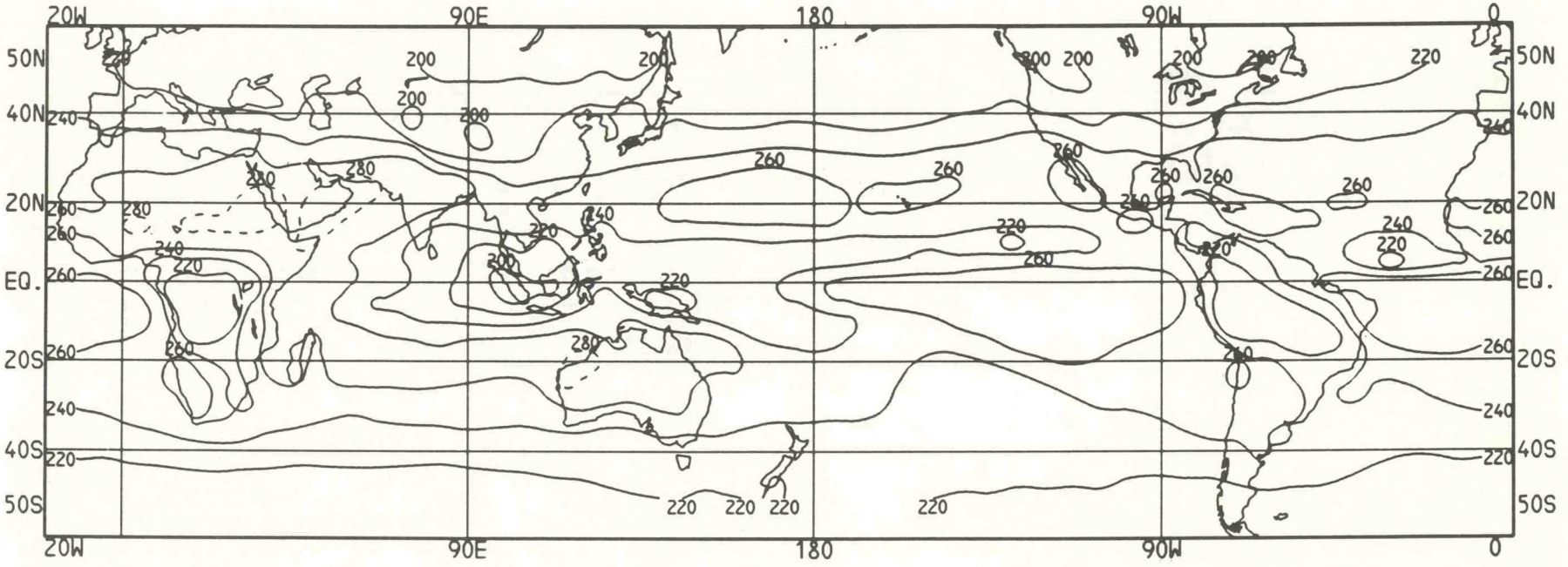

Figure 20. Same as Figure 6, except for November.

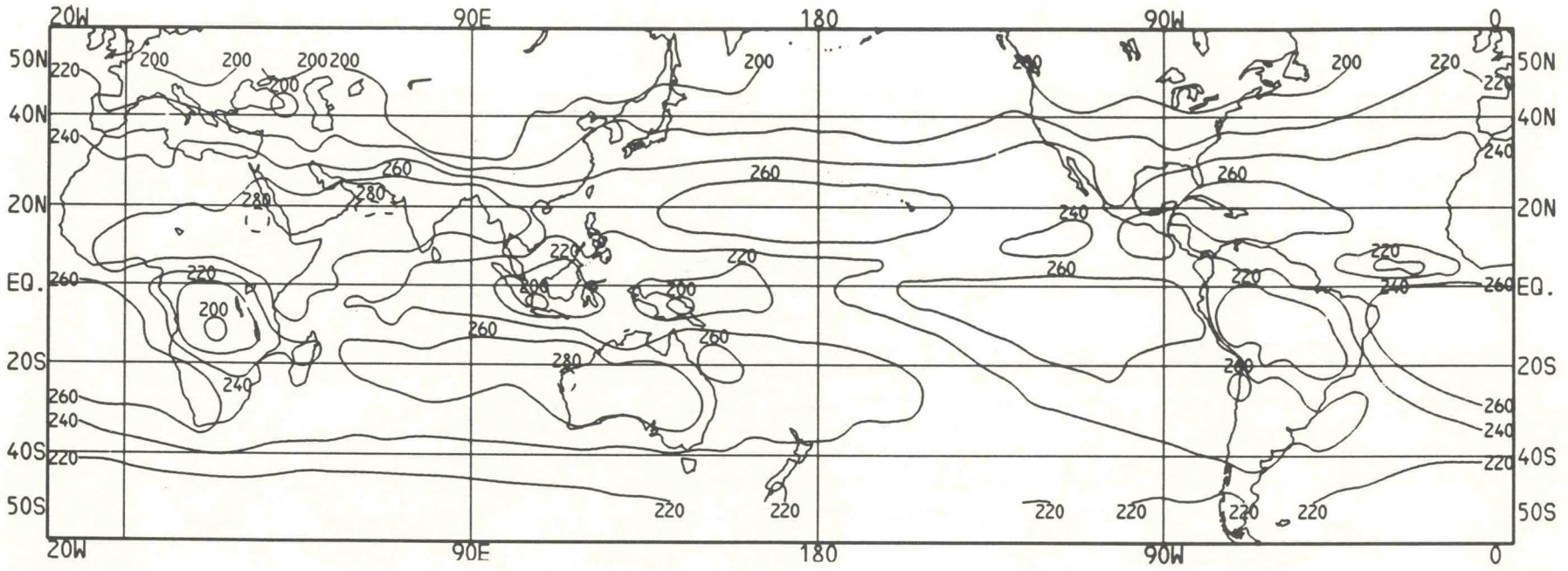

Figure 21. Same as Figure 6, except for December.

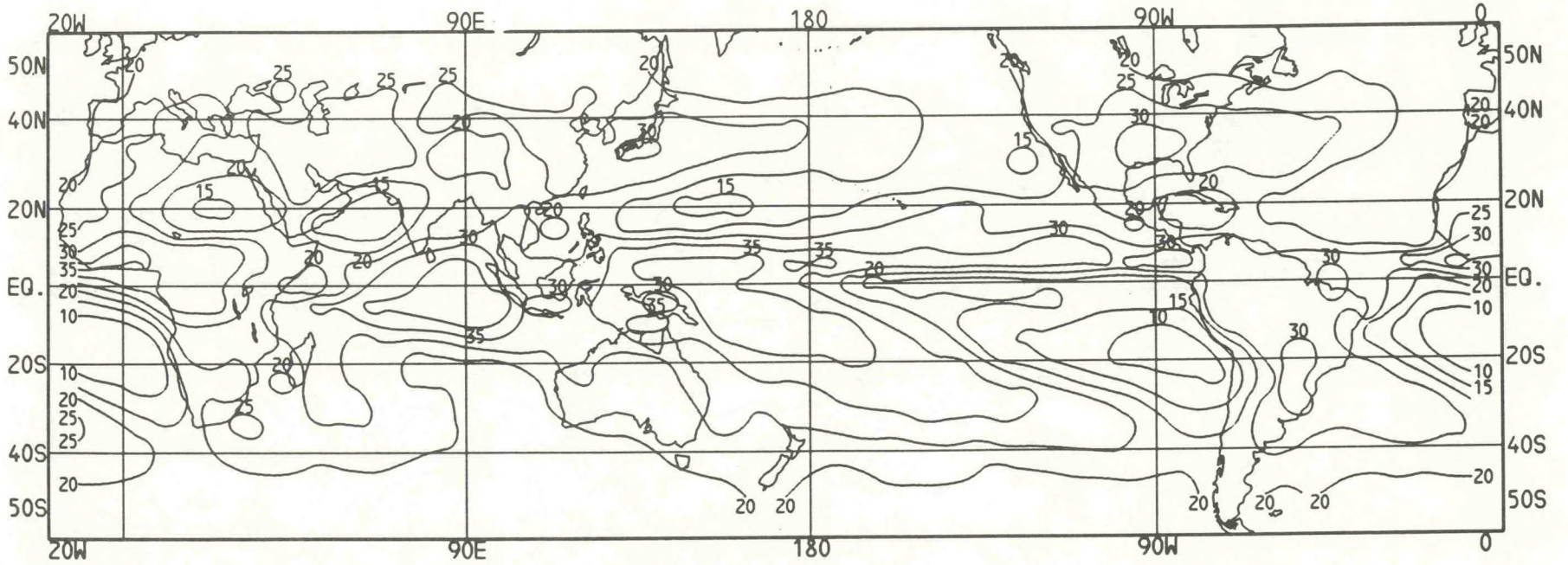

Figure 22. Spring season average standard deviation of the OLR for the period June, 1974 through November, 1983. The contour interval is 5 W m^{-2}. The day and night observations have been averaged.

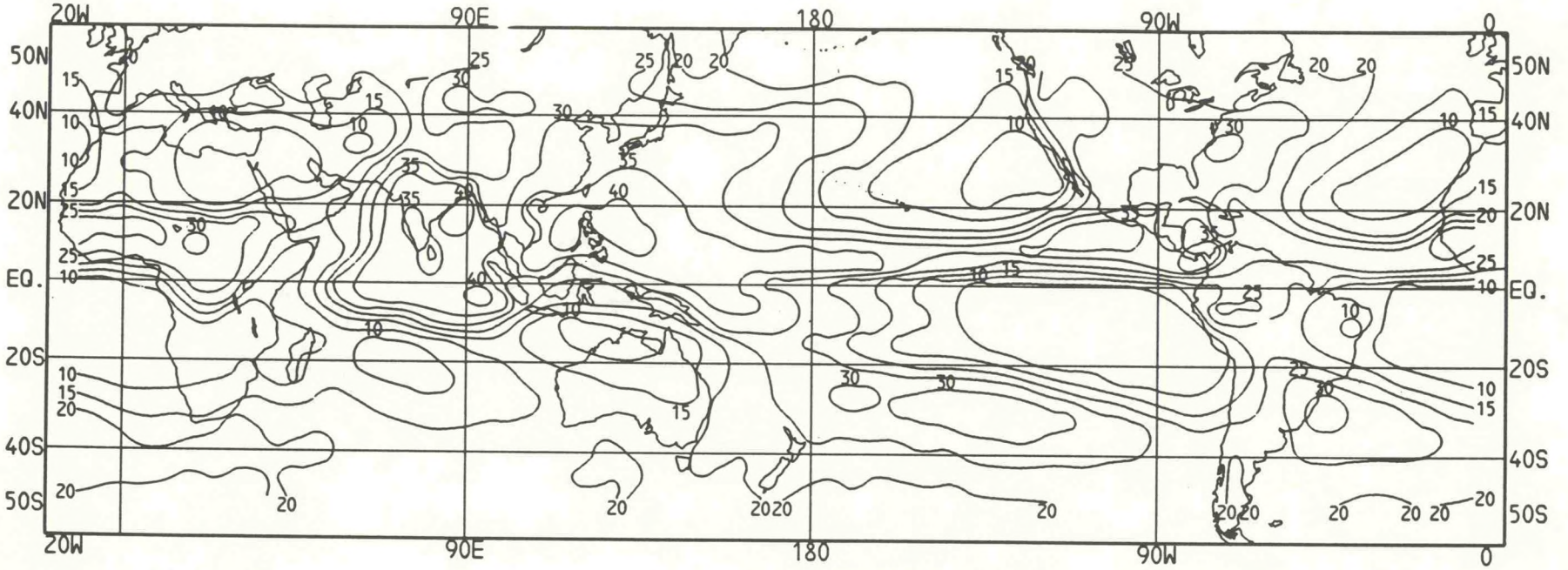

Figure 23. Same as Figure 22, except for summer season.

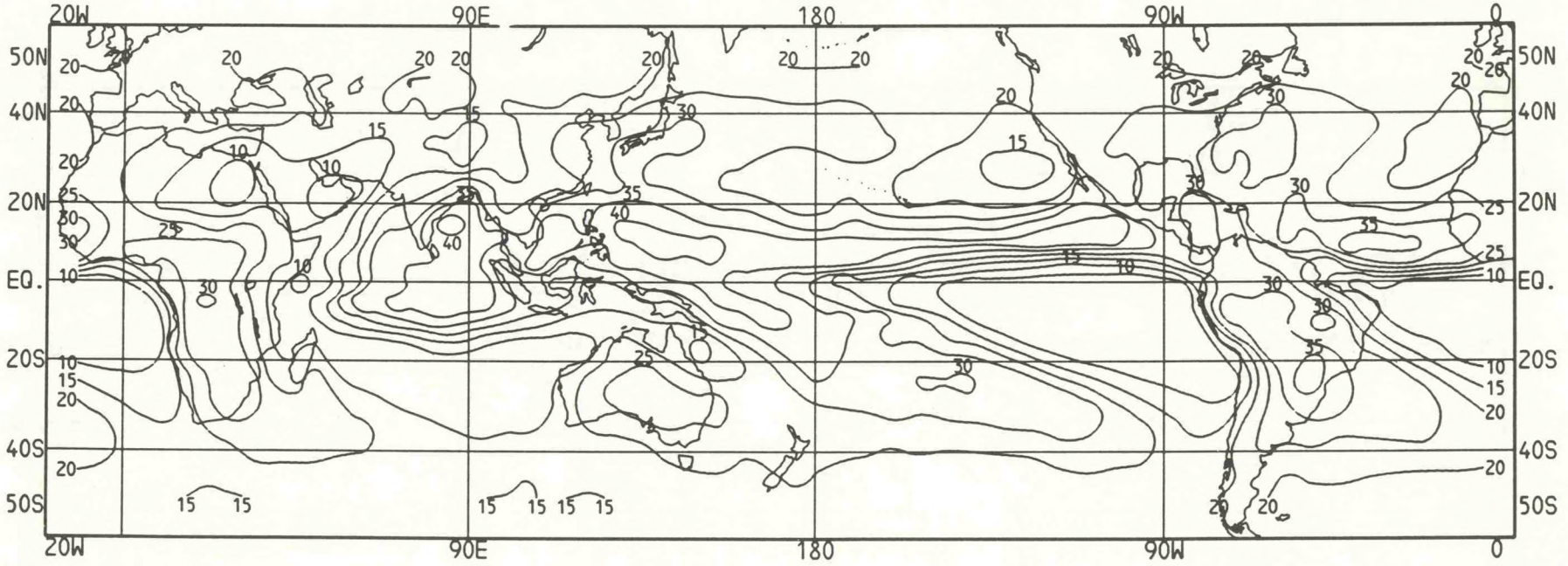

Figure 24. Same as Figure 22, except for autumn season.

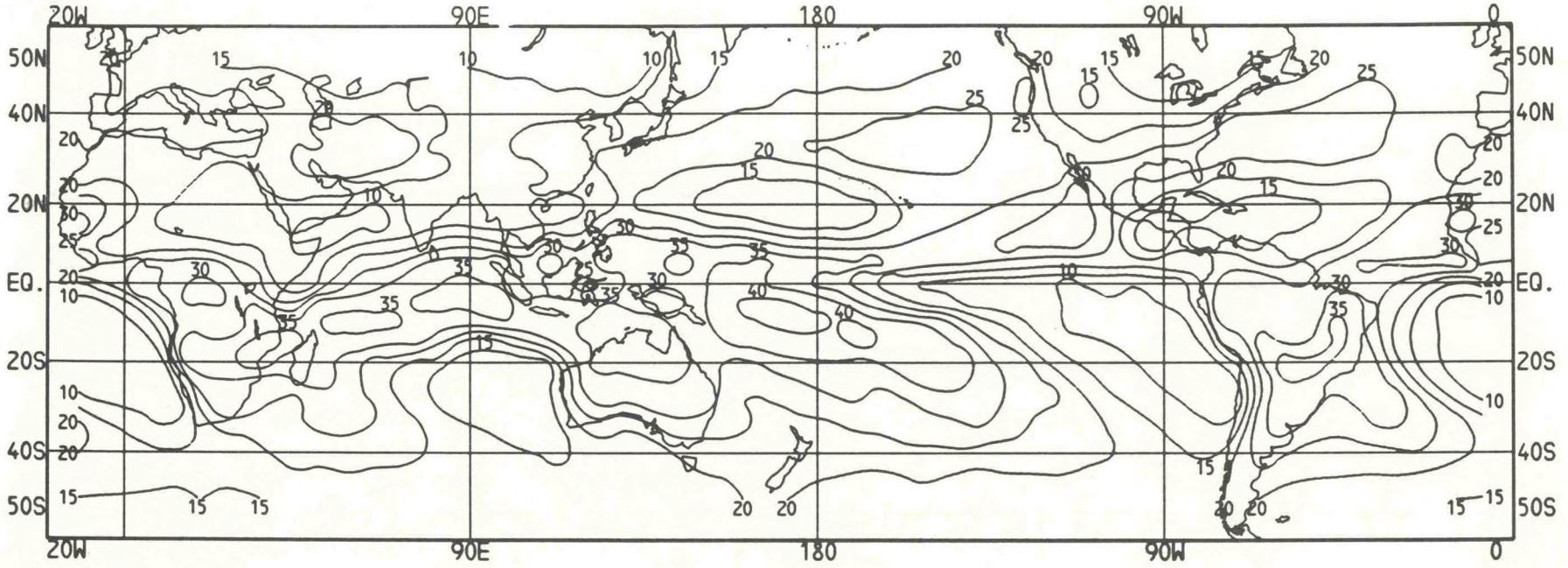

Figure 25. Same as Figure 22, except for winter season.

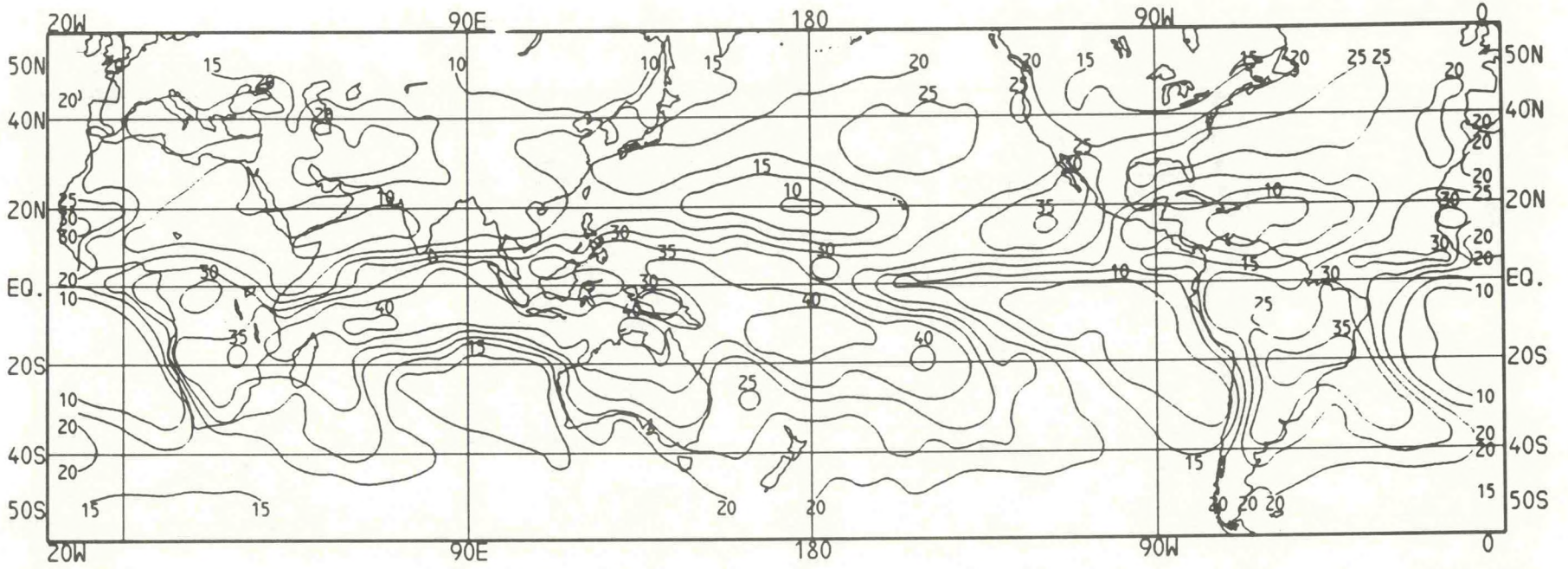

Figure 26. Same as Figure 22, except for January.

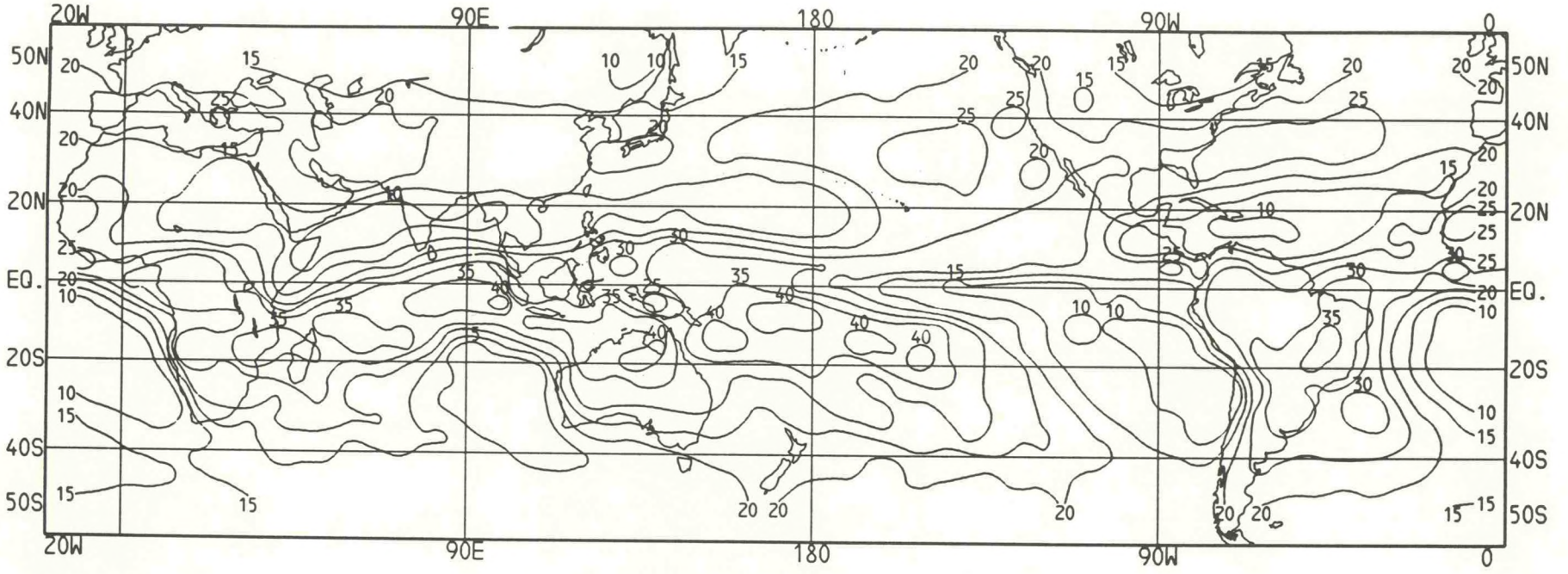

Figure 27. Same as Figure 22, except for Febuary.

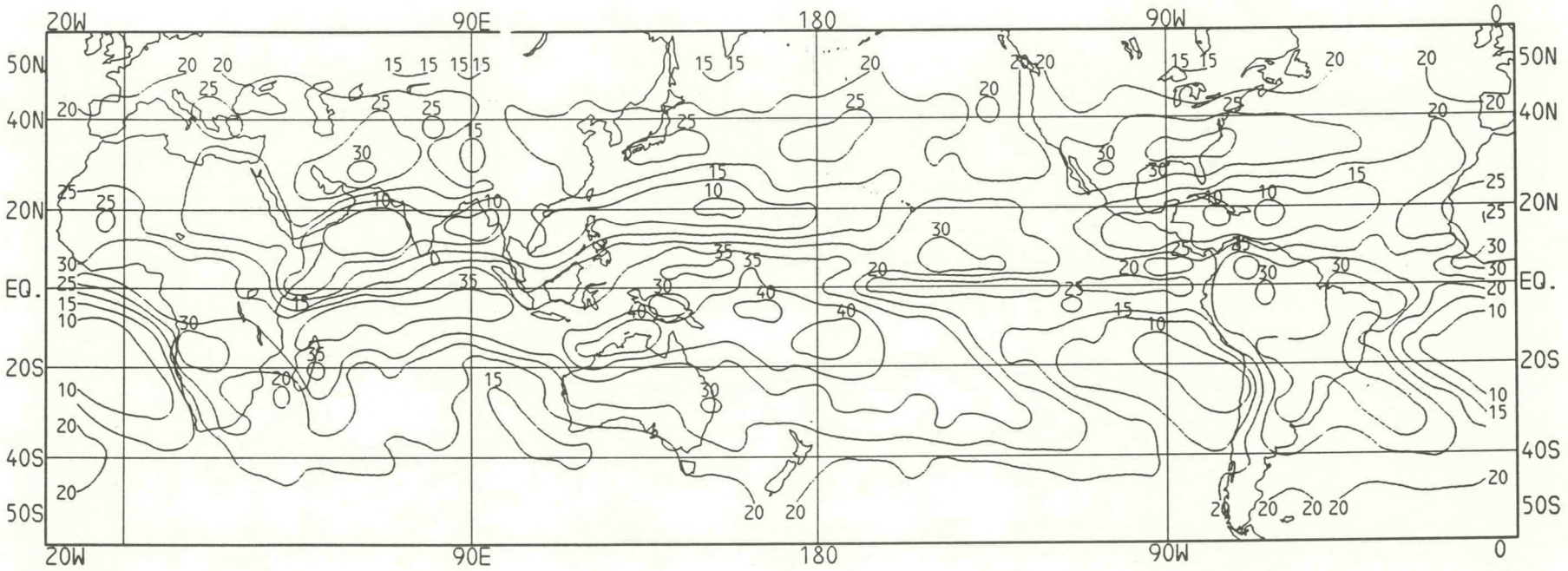

Figure 28. Same as Figure 22, except for March.

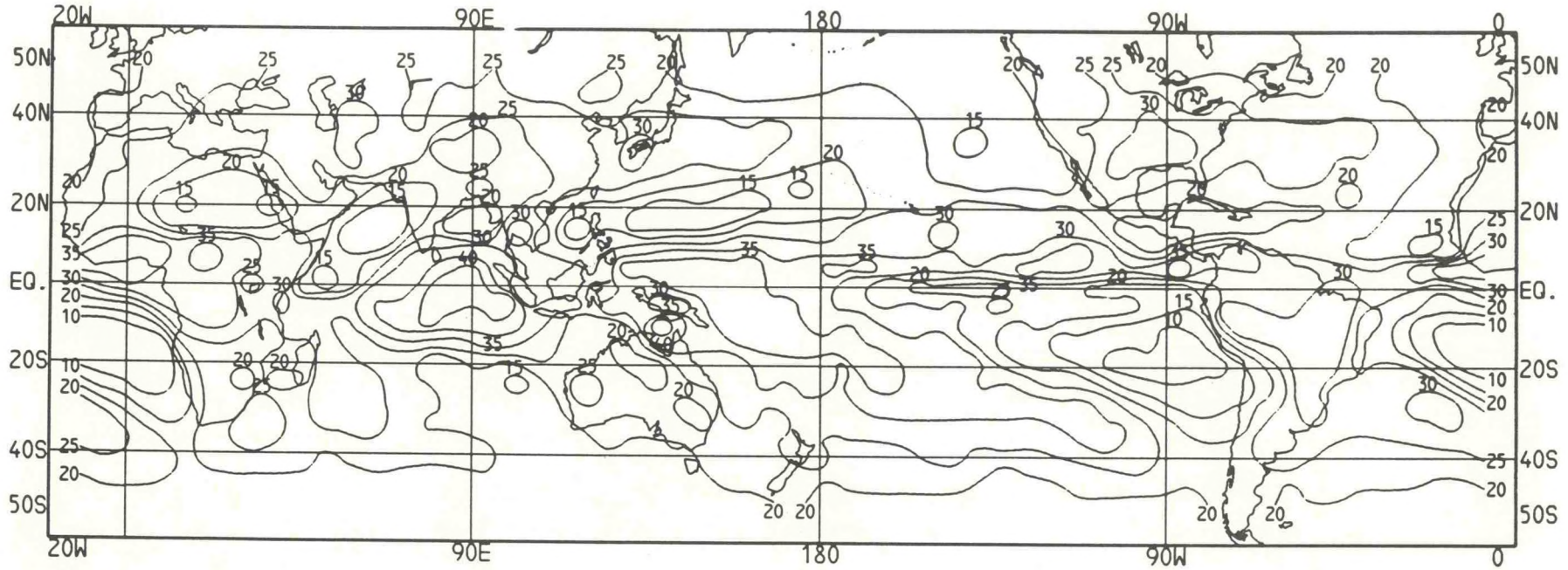

Figure 29. Same as Figure 22, except for April.

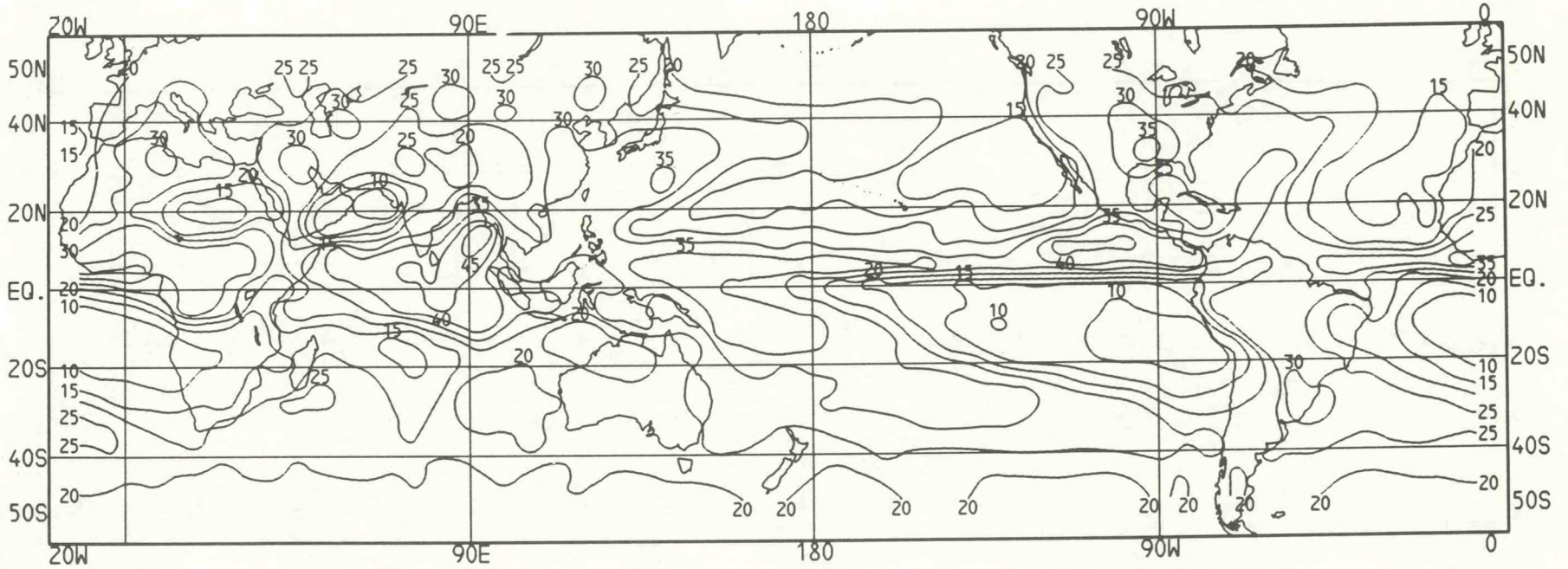

Figure 30. Same as Figure 22, except for May.

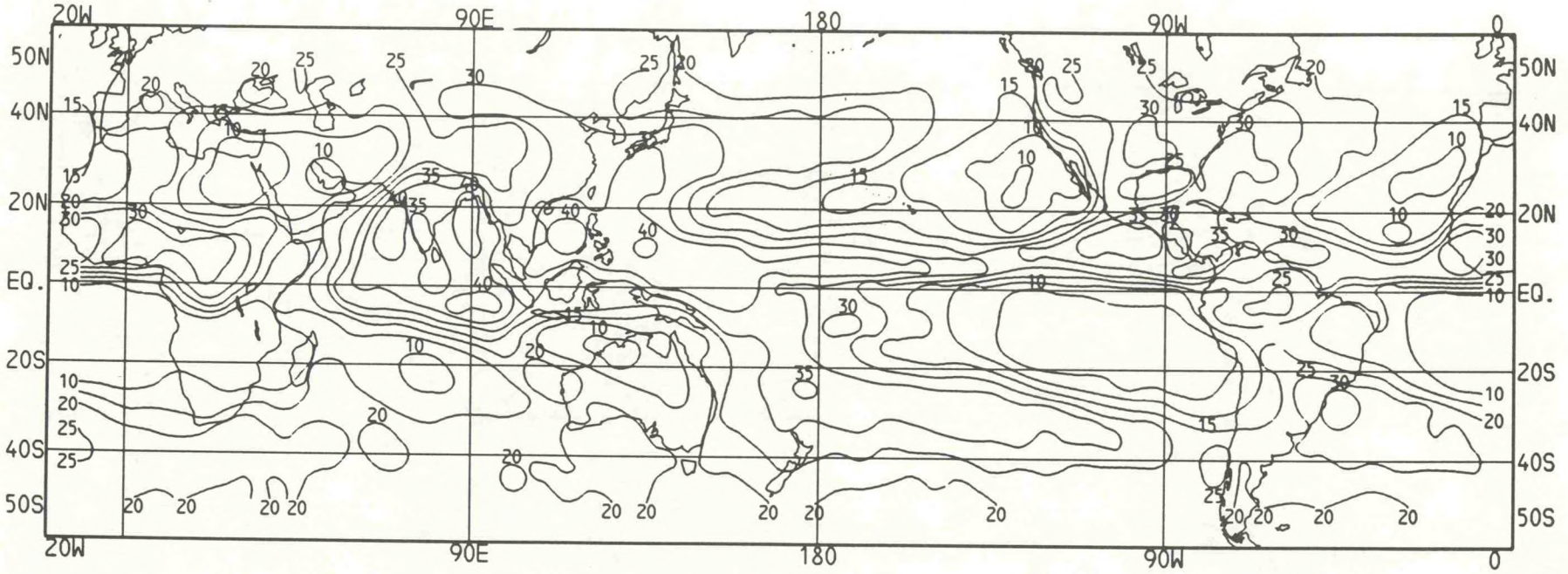

Figure 31. Same as Figure 22, except for June.

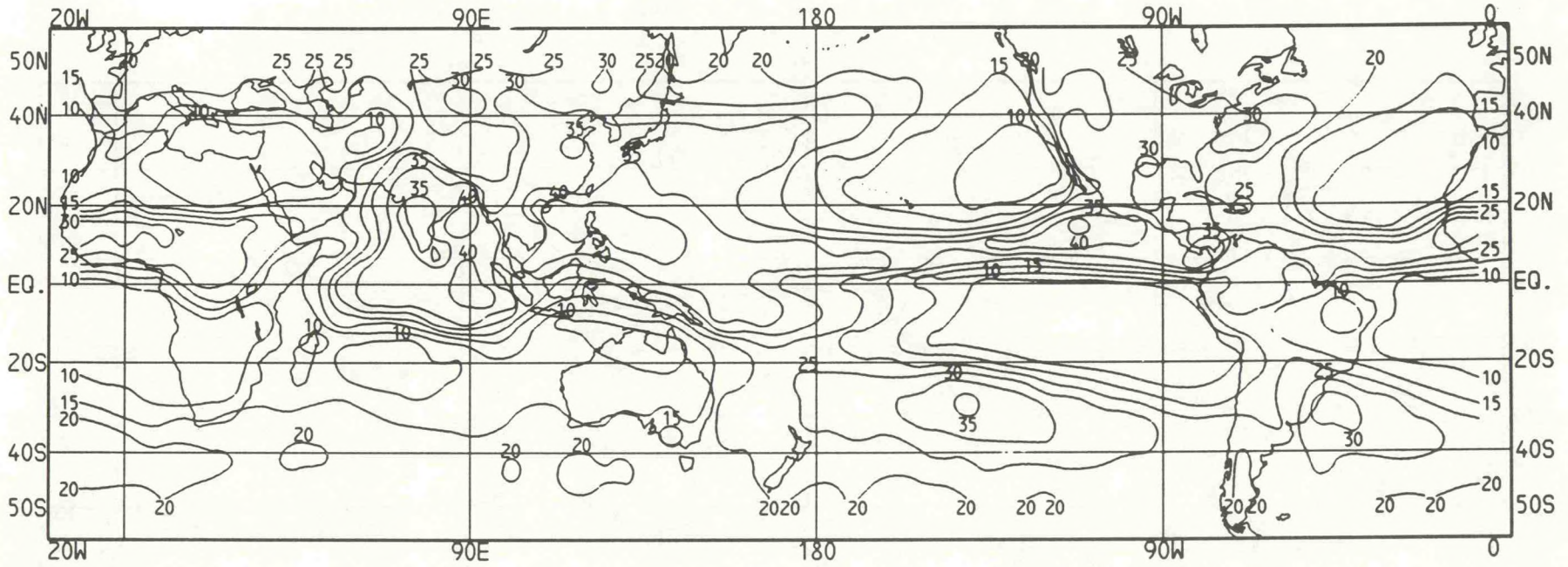

Figure 32. Same as Figure 22, except for July.

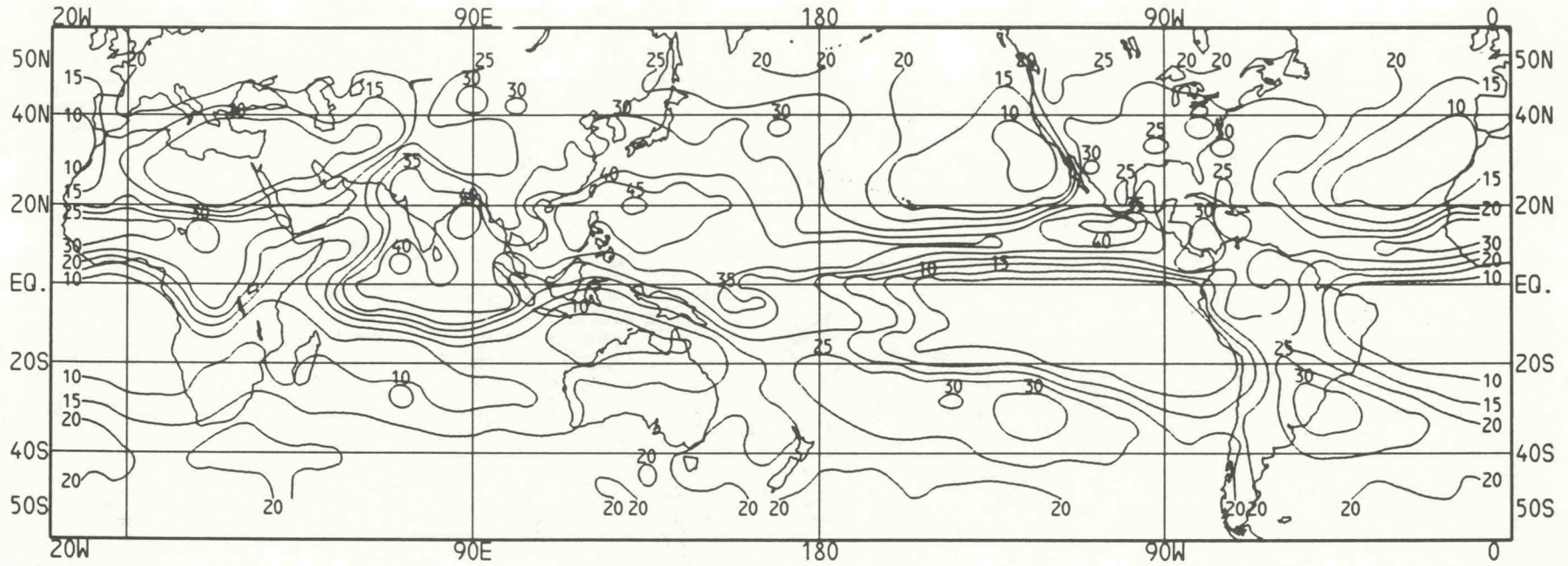

Figure 33. Same as Figure 22, except for August

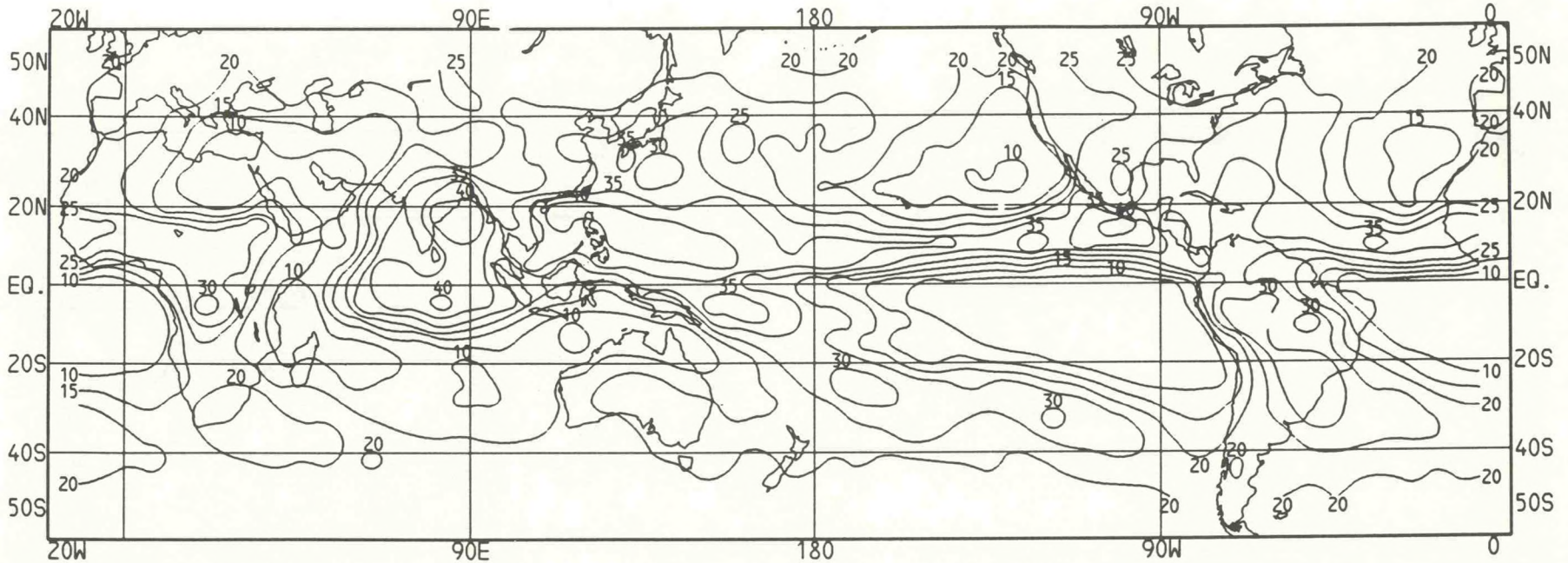

Figure 34. Same as Figure 22, except for September.

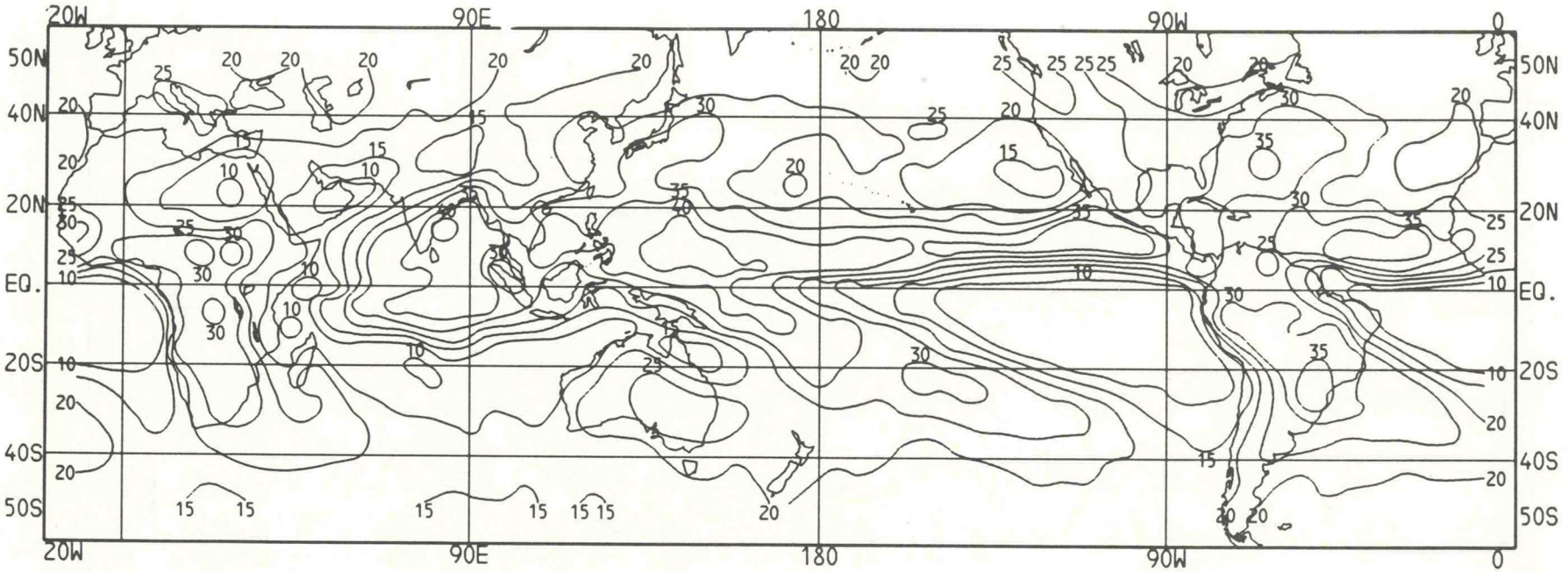

Figure 35. Same as Figure 22, except for October.

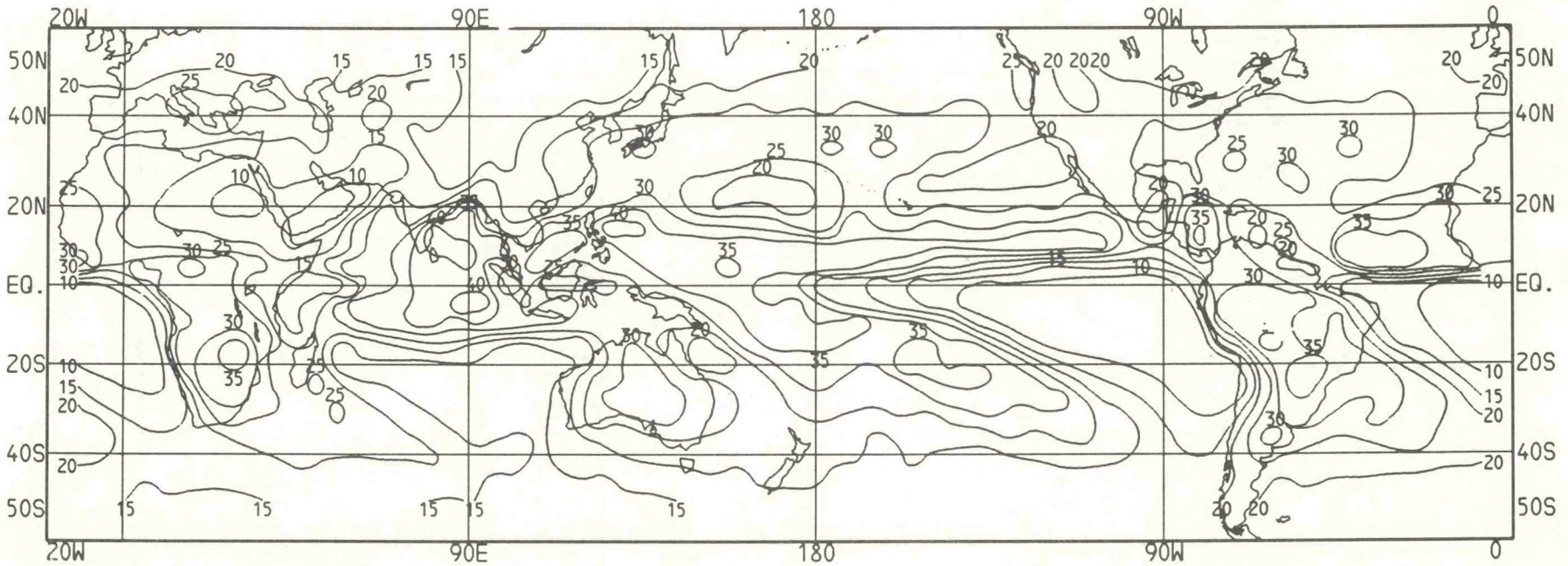

Figure 36. Same as Figure 22, except for Novermber.

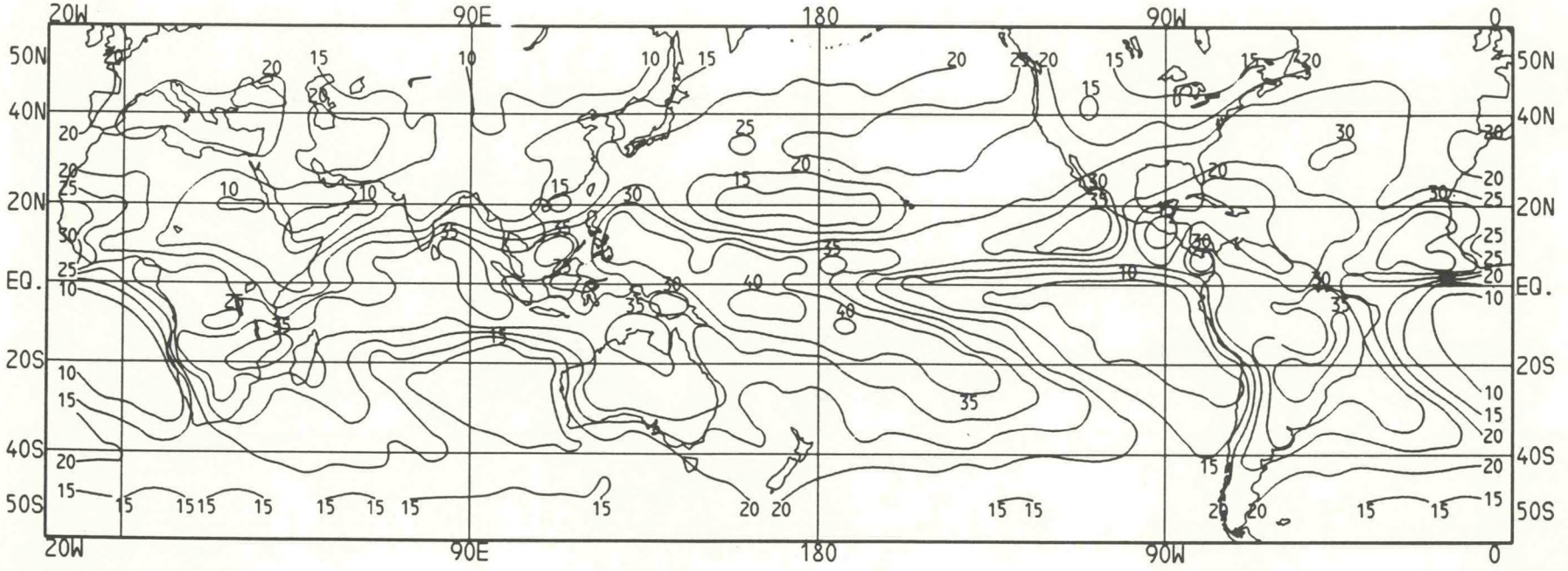

Figure 37. Same as Figure 22, except for December.